

Role of polarizations and spin-spin correlations of W 's in $e^-e^+ \rightarrow W^-W^+$ at $\sqrt{s} = 250$ GeV to probe anomalous W^-W^+Z/γ couplings

Amir Subba^{*} and Ritesh K. Singh[†]

Department of Physical Sciences, Indian Institute of Science Education and Research Kolkata,
Mohanpur 741246, India

 (Received 19 January 2023; accepted 27 March 2023; published 18 April 2023)

We study anomalous W^-W^+Z/γ couplings due to dimension-6 operators in the production process $e^-e^+ \rightarrow W^-W^+$ followed by semileptonic decay using polarizations and spin-spin correlations of W bosons. The construction of some of the polarization and spin-spin correlation asymmetries required one to distinguish between two decay quarks coming from W^+ decay. We developed an artificial neural network and a boosted decision tree to distinguish down-type jets from up-type jets and used them to put constraints on anomalous couplings at the International Linear Collider (ILC) running at $\sqrt{s} = 250$ GeV with integrated luminosities of $\mathcal{L} \in \{100 \text{ fb}^{-1}, 250 \text{ fb}^{-1}, 1000 \text{ fb}^{-1}, 3000 \text{ fb}^{-1}\}$. We find that the use of polarization and spin-correlation observables, on top of the cross sections, significantly improves the limits on anomalous coupling compared to the earlier studies.

DOI: [10.1103/PhysRevD.107.073004](https://doi.org/10.1103/PhysRevD.107.073004)

I. INTRODUCTION

The $SU(3)_c \times SU(2)_L \times U(1)_Y$ group structure of Standard Model (SM) predicts self-interactions of weak gauge bosons. The predicted self-interactions, i.e., triple and quartic gauge-boson couplings, provide a unique testing ground for new fundamental interactions. The couplings related to fermions with gauge bosons predicted by SM are experimentally confirmed by various experiments to high accuracy. With the discovery of SM-like Higgs boson at LHC [1,2], the particle spectrum of SM is complete. Though SM remains the best-tested theory for the particle and their interactions to date, we have a growing plethora of phenomena that remain unexplained in the domain of SM. It is known [3] that nearly 80% of matter of our Universe is dark matter, and till now, the detailed structure of the dark matter is still a mystery. The recently reported mass of W bosons [4] and the magnetic moment of muons [5] are in tension with the predictions of SM. All these results, along with the theoretical naturalness in the mass of the Higgs boson, do tell us that the SM is

incomplete and the fundamental theory is still lurking in the dark. However, experiments have failed to produce any significant evidence for the many explicit models of physics beyond the SM (BSM) viz. supersymmetry, models with universal extra dimensions (UED), technicolor, and so on. As a result, one moves to a model-independent way to search for a wide range of possible BSM effects. We follow a model-independent way of expanding SM called effective field theory (EFT). In this approach, SM is extended by nonrenormalizable gauge-invariant operators with mass dimensions $D > 4$, which encodes the effects of new particles with the mass scale Λ much larger than the W -boson mass m_W . All the higher-dimensional operators are constructed out of the SM fields assuming the new physics is too heavy that we can integrate them out of the Lagrangian. Assuming lepton-number conservation, the effective Lagrangian is written as [6]

$$\mathcal{L}_{\text{EFT}} = \mathcal{L}_{\text{SM}} + \frac{1}{\Lambda^2} \sum_i c_i^{(6)} \mathcal{O}_i^{(6)} + \frac{1}{\Lambda^4} \sum_j c_j^{(8)} \mathcal{O}_j^{(8)} + \dots, \quad (1)$$

where $c_i^{(6,8)}$ are Wilson's Coefficient or the couplings of the higher-dimension operators. The effects of the new physics are translated to the weak scale via these Wilson coefficients. In this paper, we study dimension-6 effective operators which gives the anomalous triple-gauge couplings (WWV , $V \in Z, \gamma$) and constrain those couplings [$c_i^{(6)}$]. Considering both CP -even and odd, the relevant dimension-6 effective operators in the HISZ basis contributing to the WWV couplings are [7,8]

^{*}as19rs008@iiserkol.ac.in

[†]ritesh.singh@iiserkol.ac.in

Published by the American Physical Society under the terms of the [Creative Commons Attribution 4.0 International license](https://creativecommons.org/licenses/by/4.0/). Further distribution of this work must maintain attribution to the author(s) and the published article's title, journal citation, and DOI. Funded by SCOAP³.

$$\begin{aligned}
\mathcal{O}_{WWW} &= \text{Tr}[W_{\nu\rho}W^{\mu\nu}W_\rho^\mu], \\
\mathcal{O}_W &= (D_\mu\Phi)^\dagger W^{\mu\nu}(D_\nu\Phi), \\
\mathcal{O}_B &= (D_\mu\Phi)^\dagger B^{\mu\nu}(D_\nu\Phi), \\
\mathcal{O}_{W\bar{W}W} &= \text{Tr}[W_{\mu\nu}W^{\nu\rho}W_\rho^\mu], \\
\mathcal{O}_{\bar{W}} &= (D_\mu\Phi)^\dagger \tilde{W}^{\mu\nu}(D_\nu\Phi),
\end{aligned} \tag{2}$$

where $\Phi = (\phi_0^+)$ is the Higgs double field and $W^{\mu\nu}, B^{\mu\nu}$ represents the field strengths of W and B gauge fields, respectively and are defined as

$$\begin{aligned}
D_\mu &= \partial_\mu + \frac{i}{2}g\tau^i W_\mu^i + \frac{i}{2}g'B_\mu, \\
W_{\mu\nu} &= \frac{i}{2}g\tau^i(\partial_\mu W_\nu^i - \partial_\nu W_\mu^i + g\epsilon_{ijk}W_\mu^i W_\nu^j), \\
B_{\mu\nu} &= \frac{i}{2}g'(\partial_\mu B_\nu - \partial_\nu B_\mu).
\end{aligned}$$

The first three operators are C and P conserving, and the last two violate C and/or P . All these operators of Eq. (2) after electroweak symmetry breaking (EWSB) give rise to non-standard triple-gauge couplings. Conventionally the WWV vertices are parametrized by the effective Lagrangian [7,9]

$$\begin{aligned}
\mathcal{L}_{\text{eff}}^{WWV} &= ig_{WWV} \left[g_1^V (W_\mu^+ W^{-\mu} - W^{+\mu} W_{\mu}^-) V^\nu + k_V W_\mu^+ W_\nu^- V^{\mu\nu} + \frac{\lambda_V}{m_W^2} W_\mu^{\nu+} W_\nu^{-\rho} V_\rho^\mu + ig_4^V W_\mu^+ W_\nu^- (\partial^\mu V^\nu + \partial^\nu V^\mu) \right. \\
&\quad \left. - ig_5^V \epsilon^{\mu\nu\rho\sigma} (W_\mu^+ \partial_\rho W_\nu^- - \partial_\rho W_\mu^+ W_\nu^-) V_\sigma + \tilde{k}_V W_\mu^+ W_\nu^- \tilde{V}^{\mu\nu} + \frac{\tilde{\lambda}_V}{m_W^2} W_\mu^{\nu+} W_\nu^{-\rho} \tilde{V}_\rho^\mu \right]
\end{aligned} \tag{3}$$

with $g_{WW\gamma} = -e$ and $g_{WWZ} = -e \cot\theta_W$ and dual field $\tilde{V}^{\mu\nu} = 1/2\epsilon^{\mu\nu\rho\sigma} V_{\rho\sigma}$, where $\epsilon^{\mu\nu\rho\sigma}$ is the Levi-Civita tensor with standard convention, $\epsilon^{0123} = 1$. The first three terms of Eq. (3) respect C and P , and the remaining four violate C and/or P . Within the SM, the couplings are given by $g_1^V = k_V = 1$, and other couplings are zero. While the value of g_1^V, g_4^V, g_5^V are fixed by the electromagnetic gauge invariance, the presence of the operators $\mathcal{O}_{WWW}, \mathcal{O}_W, \mathcal{O}_B, \mathcal{O}_{\bar{W}}, \mathcal{O}_{W\bar{W}W}$ in the effective Lagrangian will change the other values to [9]

$$\begin{aligned}
g_1^Z &= 1 + c_W \frac{m_Z^2}{2\Lambda^2}, \\
k_Z &= 1 + [c_W - s_W^2(c_B + c_W)] \frac{m_Z^2}{2\Lambda^2}, \\
k_\gamma &= 1 + (c_B + c_W) \frac{m_W^2}{2\Lambda^2}, \\
\lambda_\gamma &= \lambda_Z = c_{WWW} \frac{3m_W^2 g^2}{2\Lambda^2}, \\
g_4^Z &= g_5^Z = 0, \\
\tilde{k}_Z &= -c_{\bar{W}} s_W^2 \frac{m_Z^2}{2\Lambda^2}, \\
\tilde{k}_\gamma &= c_{\bar{W}} \frac{m_W^2}{2\Lambda^2}, \\
\tilde{\lambda}_\gamma &= \tilde{\lambda}_Z = c_{\widetilde{WWW}} \frac{3m_W^2 g^2}{2\Lambda^2},
\end{aligned} \tag{4}$$

with $s_W = \sin\theta_W$.

The anomalous WWZ/γ vertex has been studied extensively at phenomenological and experimental levels. The phenomenological studies are done at the e^-e^+ collider [10–21], the Large Hadron Collider [20,22–36], and the

Large Hadron electron Collider (LHeC) [37–41]. On the experimental side, many results are reported by different experiments like the e^-e^+ Collider [22,42–47], CMS [48–60], ATLAS [61–68], and Tevatron [69–75]. We list the best constrained values for various anomalous couplings (c_i) obtained experimentally in Table I accordingly.

The limits given in Table I are obtained by varying one parameter at a time, and others are kept at zero (SM value). It has been shown in Ref. [11] that using the polarized beam in e^-e^+ collider, some of the anomalous couplings are constrained better. In our current article, we construct spin-related observables like polarization asymmetries and spin-spin correlation asymmetries along with a cross section to constrain the above discussed anomalous couplings. The use of asymmetries will bring the directional limits on various couplings, resulting in better constraining anomalous couplings.

We probe W^-W^+ production process in the e^-e^+ collider at $\sqrt{s} = 250$ GeV using unpolarized beams, and the W 's are decayed semileptonically such that the whole process is defined as

$$e^- + e^+ \rightarrow W^- W^+ \rightarrow l^- \nu_l j j. \tag{5}$$

TABLE I. The list of tightest constraints observed on the effective operators in $SU(2) \times U(1)$ gauge at 95% CL from various experiments.

$c_i^\mathcal{O}$	Limits (TeV ⁻²)	Remarks
c_{WWW}/Λ^2	[-0.90, +0.91]	CMS [49]
c_W/Λ^2	[-2.5, +0.3]	CMS [48]
c_B/Λ^2	[-8.78, +8.54]	CMS [57]
$c_{\bar{W}}/\Lambda^2$	[-20.0, +20.0]	CMS [49]
$c_{\widetilde{WWW}}/\Lambda^2$	[-0.45, +0.45]	CMS [49]

Here $l^- \in (e^-, \mu^-)$ and j 's are the light quarks viz. $u\bar{d}/c\bar{s}$. The production process $e^-e^+ \rightarrow W^-W^+$ proceeds through one neutrino mediated t -channel and two γ^*/Z mediated s -channels. The s -channel diagrams contain trilinear WWV gauge boson couplings whose deviations from SM value in the presence of Lagrangian given by Eq. (3) are studied in this article. For the implementation of anomalous couplings, we create a Universal FeynRules Output (UFO) [76] model file using Eq. (3) in FeynRules [77]. The translation of couplings in Eq. (3) to dimension-6 couplings can be done using Eq. (4). We perform our analysis at the particle level, i.e., the quarks obtained at the matrix element level are allowed to undergo showering and hadronization. While constructing some spin-related asymmetries, we need the correct information of daughter particles of W boson. For that, we used machine learning (ML) techniques, particularly artificial neural network (ANN), and boosted decision trees (BDT).

In Sec. II we describe the spin, and the observables obtained using the spin of a particle. We primarily focused on the asymmetries and the spin-spin correlation asymmetries of spin-1 boson. We also list down the relevant observables affected by flavor tagging and those which are not. A method of ML techniques used for flavor tagging the jets to the light quarks is explained in Sec. III. In Sec. IV, we discuss parameter estimation and the limits obtained on the five anomalous couplings. We conclude in Sec. V.

II. SPIN AND RELATED OBSERVABLES

All the fundamental particles have a finite spin, and all the fundamental interactions conserve angular momentum. The spin of a given particle decides the Lorentz structure of the couplings it will have with other particles, hence its production and decay mechanism. A decaying particle's spin and polarization information gets encoded in the angular distribution of its decay products. One can use various kinematic distributions of decay products to decode the spin content and dynamics of any process [78]. The range

of spin and polarization sensitive observables discussed in this section are broadly divided into two classes. The first deals with asymmetries that measure various polarization parameters of a resonance. The second class involves asymmetries that probe the spin-spin correlation between two resonances. We discuss them here one by one.

A. Polarization asymmetries

Let us consider a scattering process of particles B_1 and B_2 where a resonance A of spin s along with some other particles is produced followed by its subsequent decay to a and b , shown in Fig. 1. The differential rate for such a process, assuming a narrow width approximation (NWA) for resonance A , is given as [79],

$$d\sigma = \sum_{\lambda, \lambda'} \left[\frac{(2\pi)^4}{2I_{B_1 B_2}} \rho(\lambda, \lambda') \delta^4(k_{B_1} + k_{B_2} - P_A - \sum p_i) \frac{d^3 p_A}{2E_A (2\pi)^3} \prod_i \frac{d^3 p_i}{2E_i (2\pi)^3} \right] \times \left[\frac{1}{\Gamma_A} \frac{(2\pi)^4}{2m_A} \Gamma'(\lambda, \lambda') \delta^4(P_A - P_a - P_b) \frac{d^3 p_a}{2E_a (2\pi)^3} \frac{d^3 p_b}{2E_b (2\pi)^3} \right], \quad (6)$$

where $I_{B_1 B_2}$ is the flux factor and $\lambda's, \Gamma_A, m_A$ are the helicities, total width, and mass of A , respectively. Rewriting the two terms of the differential rate in terms of polarization density, $P_A(\lambda, \lambda')$ and decay density matrix, $\Gamma_A(\lambda, \lambda')$, the decay angular distribution can be written down as

$$\frac{1}{\sigma} \frac{d\sigma}{d\Omega_a} = \frac{2s+1}{4\pi} \sum_{\lambda, \lambda'} P_A(\lambda, \lambda') \Gamma_A(\lambda, \lambda'). \quad (7)$$

The production dynamics are encoded in the given polarization density matrix and one can calculate to quantify the production rate of various quantum interference states. The general expressions for $P_A(\lambda, \lambda')$ and $\Gamma_A(\lambda, \lambda')$ for a spin-1 particle are given in Eqs. (A1) and (A2) of the Appendix, respectively. Using these expressions one can rewrite the angular distribution for a spin-1 particle as

$$\begin{aligned} \frac{1}{\sigma} \frac{d\sigma}{d\Omega_a} = & \frac{3}{8\pi} \left[\left(\frac{2}{3} - (1-3\delta) \frac{T_{zz}}{\sqrt{6}} \right) + \alpha p_z \cos \theta_a + \sqrt{\frac{3}{2}} (1-3\delta) T_{zz} \cos^2 \theta_a + \left(\alpha p_x + 2\sqrt{\frac{2}{3}} (1-3\delta) T_{xz} \cos \theta_a \right) \sin \theta_a \cos \phi_a \right. \\ & + \left(\alpha p_y + 2\sqrt{\frac{2}{3}} (1-3\delta) T_{yz} \cos \theta_a \sin \theta_a \cos \phi_a + (1-3\delta) \left(\frac{T_{xx} - T_{yy}}{\sqrt{6}} \right) \sin^2 \theta_a \cos(2\phi_a) \right) \\ & \left. + \sqrt{\frac{2}{3}} (1-3\delta) T_{xy} \sin^2 \theta_a \sin(2\phi_a) \right], \end{aligned} \quad (8)$$

where θ_a, ϕ_a are the polar and azimuthal angle of daughter a in the rest frame of the parent, A with its would be momentum along the z -axis. The initial beam direction and the A momentum in the lab frame define the x - z plane, i.e., $\phi = 0$ plane, in the rest frame of A as well. For A being a vector boson decaying to a pair of fermion through $V-A$ interaction, the parameters α and δ are given by [79]

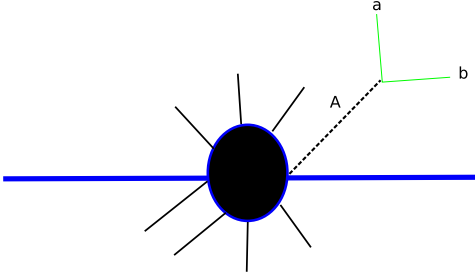


FIG. 1. Schematic diagram showing the production of a resonance A in a scattering process followed by its decay to particles a and b .

$$\alpha = \frac{2(R_a^2 - L_a^2)\sqrt{1 + (x_1^2 - x_2^2)^2 - 2(x_1^2 + x_2^2)}}{12L_a R_a x_1 x_2 + C(R_a^2 + L_a^2)^2},$$

$$\delta = \frac{4L_a R_a x_1 x_2 + (R_a^2 + L_a^2)(C - 2)}{12R_a L_a x_1 x_2 + C(R_a^2 + L_a^2)^2}, \quad (9)$$

where $C = 2 - (x_1^2 - x_2^2)^2 + (x_1^2 + x_2^2)$, $x_i = \frac{m_i}{M_A}$. In the high-energy limit, the final-state fermions ($e^\mp, \mu^\mp, u, d, c, s$) can be taken to be massless which implies $x_1 \rightarrow 0, x_2 \rightarrow 0$ and $\delta \rightarrow 0, \alpha \rightarrow \frac{R_a^2 - L_a^2}{R_a^2 + L_a^2}$. Further, for the decay of W , within the SM , $R_a = 0$ hence $\alpha = -1$. The vector \vec{p} and tensor T_{ij} polarization can be calculated from the production part. For example P_x and T_{xz} can be calculated as follows:

$$P_x = \frac{[\rho_T(+, 0) + \rho_T(0, +)] + [\rho_T(0, -) + \rho_T(-, 0)]}{\sqrt{2}\sigma},$$

$$T_{xz} = \frac{\sqrt{3}[\rho_T(+, 0) + \rho_T(0, +)] - [\rho_T(0, -) + \rho_T(-, 0)]}{4\sigma}. \quad (10)$$

All other polarizations can be found from the different combinations of density matrix and tracelessness of T_{ij} as shown in [80,81].

Similarly, at the level of decay products, one can find the same polarization parameters by using different asymmetries constructed from the decay angular distribution of fermions. Different asymmetries can be calculated using different combination of angular variables (c_j) as given below,

$$A_i = \frac{\sigma(c_j > 0) - \sigma(c_j < 0)}{\sigma(c_j > 0) + \sigma(c_j < 0)}. \quad (11)$$

Here c_j is a function of ϕ and θ of the final-state fermions. The relation of different asymmetries with the angular functions c_j is listed in Table II. The angular functions c_1 – c_3 are parity odd while c_4 – c_8 and parity even. This means that asymmetries A_1 – A_3 can be nonzero only if there is parity violation in the decay process, i.e., $\alpha \neq 0$, as these three asymmetries are

TABLE II. Table showing the asymmetries of a spin-1 particle and the angular parameters that are used to find the respective asymmetries.

A_i	c_j	Functions
A_x	$c_1 \equiv c_x$	$\sin \theta \cos \phi$
A_y	$c_2 \equiv c_y$	$\sin \theta \sin \phi$
A_z	$c_3 \equiv c_z$	$\cos \theta$
A_{xy}	$c_4 \equiv c_{xy}$	$\sin^2 \theta \sin(2\phi)$
A_{xz}	$c_5 \equiv c_{xz}$	$\sin \theta \cos \theta \cos \phi$
A_{yz}	$c_6 \equiv c_{yz}$	$\sin \theta \cos \theta \sin \phi$
$A_{x^2-y^2}$	$c_7 \equiv c_{x^2-y^2}$	$\sin^2 \theta \cos(2\phi)$
A_{zz}	$c_8 \equiv c_{zz}$	$\sin(3\theta)$

proportional to the α parameter. The other five asymmetries A_4 – A_8 are nonzero as long as the corresponding tensor polarization appearing in Eq. (8) are nonzero.

For two body decay in the rest frame, two daughters emerge in opposite directions, i.e., if we average over them, then the asymmetries A_1 – A_3 will vanish. In other words, to construct the vector polarizations \vec{p} we need to be able to distinguish between two daughters. This is possible in the leptonic decays of W^\pm but for the hadronic decay channels, we need a method to identify (tag) them. This issue is addressed in Sec. III.

B. Spin-spin correlation

For a polarization asymmetry to be nonzero, we need the corresponding particle being produced with nonzero polarization. In the case of an unpolarized beam collisions producing a pair of fermions, we require parity violation in the production process to have a nonzero polarization. But for $t\bar{t}$ pair production at LHC through QCD interactions, we have no parity violation and hence unpolarized top-quarks. However, due to the vectorial nature of the gluons interaction with top-quark one has a certain kind of spin-spin correlations between t and \bar{t} spins. And experiments [75,82,83] have shown the spin correlations in $t\bar{t}$ systems. These additional sets of observables will provide an additional probe for the possible NP signal. The spin-spin correlation asymmetries can be calculated in the similar fashion as we have shown for single particle calculations of asymmetries. We consider a generic scattering process in which two spin full resonance is produced, followed by its decay as shown in Fig. 2. The differential rate for this process would remain similar to Eq. (8) but with few changes; the single particle density matrix $\rho(\lambda, \lambda')$ is replaced with two particle density matrix $\rho(\lambda_A, \lambda'_A, \lambda_B, \lambda'_B)$ and there is an additional factor of square bracket terms containing $\Gamma(\lambda, \lambda)$ one for decay of particle A and another for particle B . The full-spin correlated polarization density matrix for a pair of spin-1 particles defined as

$$P_{AB}(\lambda_A, \lambda'_A, \lambda_B, \lambda'_B) = \rho(\lambda_A, \lambda'_A, \lambda_B, \lambda'_B) / \text{Tr}(\rho)$$

can be parametrized in terms of polarizations and spin correlation variables as [81]

$$\begin{aligned} P_{AB}(\lambda_A, \lambda'_A, \lambda_B, \lambda'_B) = & \frac{1}{9} \left[I_{3 \times 3} \otimes I_{3 \times 3} + \frac{3}{2} \vec{p}^A \cdot \vec{S} \otimes I_{3 \times 3} + \frac{3}{2} I_{3 \times 3} \otimes \vec{p}^B \cdot \vec{S} + \sqrt{\frac{3}{2}} T_{ij}^A (S_i S_j + S_j S_i) \otimes I_{3 \times 3} \right. \\ & + \sqrt{\frac{3}{2}} I_{3 \times 3} \otimes T_{ij}^B (S_i S_j + S_j S_i) + p p_{ij}^{AB} S_i \otimes S_j + p T_{ijk}^{AB} S_i \otimes (S_j S_k + S_k S_j) + T p_{ijk}^{AB} (S_i S_j + S_j S_i) \otimes S_k \\ & \left. + T T_{ijkl}^{AB} (S_i S_j + S_j S_i) \otimes (S_k S_l + S_l S_k) \right], \quad (i, j, k = x, y, z). \end{aligned} \quad (12)$$

The indices λ_A and λ'_A label the left matrices in the tensor products while λ_B and λ'_B label the right matrices. By combining Eqs. (12) and (A2), the normalized joint decay angular distribution can be written as

$$\frac{1}{\sigma} \frac{d^2 \sigma}{d\Omega_a d\Omega_b} = \left(\frac{3}{4\pi} \right)^2 \sum_{\lambda'_s} P_{AB}(\lambda_A, \lambda'_A; \lambda_B, \lambda'_B) \quad \Gamma_A(\lambda_A, \lambda'_A) \Gamma_B(\lambda_B, \lambda'_B), \quad (13)$$

where $d\Omega_a$ and $d\Omega_b$ are the solid angle measure for the decay product A and B particle. To compute the various polarization and spin correlation parameters appearing in Eq. (12) we can define asymmetries similar to Eqs. (10) and/or (11) as described in detail in Ref. [81]. For the present work, we choose to discuss the asymmetries defined using angular distribution Eq. (13) of the final-state decayed particles. The set of spin-correlation asymmetries can be defined as

$$A_{ij}^{AB} = \frac{\sigma(c_i^a c_j^b > 0) - \sigma(c_i^a c_j^b < 0)}{\sigma(c_i^a c_j^b > 0) + \sigma(c_i^a c_j^b < 0)}, \quad (14)$$

where $i, j \in (1..8)$ and the parameters c 's can be read out from the previous section. These asymmetries probe the spin correlation parameters like: $p p_{ij}^{AB}$, $p T_{ij}^{AB}$, $T p_{ij}^{AB}$, and $T T_{ij}^{AB}$ which are vector-vector, vector-tensor, tensor-vector, and

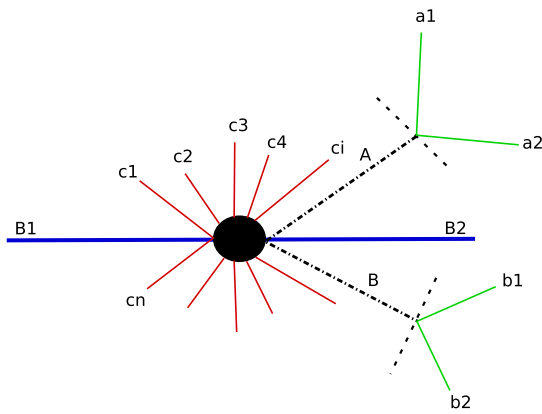


FIG. 2. Schematic diagram showing the production of two resonance A and B followed by their decay to $a_1 a_2$ and $b_1 b_2$, respectively.

tensor-tensor correlations, respectively. For example, A_{13}^{AB} probes $p p_{xz}^{AB}$, A_{14}^{AB} probes $p T_{xxy}$ correlation parameters, etc.

Furthermore, the angular functions c_1 , c_2 , and c_3 require the identification of the flavor of the daughter particles; hence, some of the spin-correlation asymmetries will vanish if we average over the flavor in the case of hadronic decay of W^\pm . Thus, for the semileptonic final state that we are considering in this work, it is of utmost importance to do flavor tagging to be able to construct all the asymmetries. Additionally the angular functions c_2 , c_4 , and c_6 are CP -odd, so the corresponding polarization asymmetries are expected to be zero for the CP -conserving production processes. In this case all the spin-correlation having one (and exactly one) factor of CP -odd angular the function will also vanish. Examples are A_{12} , A_{34} , etc. However the correlation asymmetries depending upon two of the CP -odd angular functions are CP -even and will be nonzero in general, even in the absence of CP -violation in the production process. The CP properties of all the polarization and spin correlation asymmetries are listed in Fig. 3 with letters ‘‘E’’ and ‘‘O’’ denotes CP -even and -odd, respectively. The asymmetries that require flavor reconstructions are marked in light red color and the asymmetries that are immune to the flavor are marked in light blue. There are a total of 25 spin correlation asymmetry and ten polarization asymmetry that is independent of flavor tagging, while there are 39 spin correlation asymmetries and six polarization asymmetries that will vanish without flavor tagging. The flavor tagging is trivial in the leptonic branch and very obscure in the hadronic branch. In the next section, we try to use machine learning methods to train models (tagger) to tag the light quark flavors for our purpose in

σ	A_x	A_y	A_z	A_{xy}	A_{xz}	A_{yz}	$A_{x^2-y^2}$	A_{zz}
A_x	E	O	E	O	E	O	E	E
A_y	O	E	O	E	O	E	O	O
A_z	E	O	E	O	E	O	E	E
A_{xy}	O	E	O	E	O	E	O	O
A_{xz}	E	O	E	O	E	O	E	E
A_{yz}	O	E	O	E	O	E	O	O
$A_{x^2-y^2}$	E	O	E	O	E	O	E	E
A_{zz}	E	O	E	O	E	O	E	E

FIG. 3. Table of polarization asymmetries (first row and first column) and spin correlation asymmetries (all others) along with their CP parities. For spin correlation asymmetries “E” stands for CP -even and “O” for CP -odd. The polarization asymmetries linear in y are also CP -odd and others are CP -even. The light red color indicates that the asymmetries require flavor tagging, and light blue indicates immunity to the flavors.

the $e^-e^+ \rightarrow W^-W^+$ process with W^- decaying leptonically and W^+ decaying hadronically.

III. FLAVOR TAGGING

We need to develop a light flavor tagger for W 's decaying hadronically to exploit all the asymmetries. For that, we developed an artificial neural network and boosted decision tree. These kinds of techniques have long been used in the field of high-energy physics. It was used for track reconstruction in wire chambers [84] and cluster finding in cellular calorimeters [85]. The ML technique is also applied extensively to classify the jets initiated by quarks and gluon [86–94]. A similar algorithm can be used for flavor tagging to distinguish the jets initiated by heavy or light quarks or gluons [95–99]. The jet images are also used by the ML algorithm to tag electroweak or QCD jets [100,101]. A similar technique can be used to distinguish between the electroweak bosons ($W^+/W^-, W/Z$) [102]; this can be further utilized for studying the fully hadronic channel of W^+W^- which receives a large background contribution from $ZZ \rightarrow$ hadrons. While studying BSM models or finding rare particles which require solving difficult signal versus background classification problems, ML techniques are used [103–114]. We can also use such ML methods to correctly identify the nature and properties

of outgoing particles from high-energy collisions [115–117]. In our study, the W^+ boson decays to light quarks ($u\bar{d}/c\bar{s}$), and due to the similar signature of the jets produced from these light quarks, it is nontrivial to tag the jets efficiently. When the W^+ boson decays hadronically, the antiquark (down-type quark) comes with the higher energy. So, if we exploit these asymmetries in energy between two types of quarks, we can correctly tag the jets roughly 75% of the time. Since the energy of final state fermions depends on the polarization of the W boson, we cannot use energy as a variable to tag the jets. We tried to classify the jets on an event-by-event basis into two classes based on the processes used: (i) c vs \bar{s} for $W^+ \rightarrow c\bar{s}$ sample, (ii) u vs \bar{d} for $W^+ \rightarrow u\bar{d}$ sample, (iii) cs vs ud , and (iv) cu vs sd for the combined sample. We train separate ANN and BDT models for each of the four cases.

We used MadGraph5_aMC@NLO [118] for event generation. The process generated is

$$e^- + e^+ \rightarrow W^- + W^+, \quad W^- \rightarrow l^- \bar{\nu}_l, \quad W^+ \rightarrow jj, \quad (15)$$

where j are the light quarks (u, d, c, s) at a center-of-mass energy $\sqrt{s} = 250$ GeV. The events are generated using a diagonal Cabibbo-Kobayashi-Maskawa matrix. These are then passed to PYTHIA 8 [119] for showering and hadronization. The final-state particle is selected with $p_T \geq 0.3$ GeV and with $|\eta| \leq 3.0$. The lepton from the decay of W^- is excluded from further analysis. We have used two sets of jet clustering algorithms in FastJet [120,121]; firstly, the final set of particles are clustered using $\text{anti-}k_T$ jet clustering [122] with jet radius $R = 0.7$ and those $\text{anti-}k_T$ jets are further clustered using k_T algorithm [123] with jet radius $R = 1.0$, such that the excluded soft particles are also clustered. It is seen that these combinations of clustering reduce the number of jets in each event. We have found that the first two hardest jets amount to approximately 90% of all jet momentum in each event, so it makes perfect sense to work with just two hardest jets rather than the whole sets of jets. To put the *truth* label on the jet for supervised learning, we used the geometric distance ΔR_{ij} between reconstructed jets and the initial partons (quarks). Considering only two hard jets, there are four combinations:

- (1) hardest jet near up-type quark;
- (2) hardest jet near down-type quark;
- (3) both jet near up-type quark; and
- (4) both jets near down-type quark.

The first two conditions are straightforward, but for any event satisfying the third or fourth condition, we always set the hardest jet to the respective quark. Once the truth labeling is set, we obtained various parameters of jets and

the particle within the jets to make them as input for different ML models. We choose the following features for each of the jets:

- (i) Total number of leptons (`nlep`);
- (ii) Total energy of positive and negative leptons (`e1+`, `e1-`);
- (iii) Total number of hadrons (`nhad`), total energy of hadrons (`ehad`);
- (iv) Total number of charged hadrons (`nChad`) and the total energy of positive and negative hadrons (`ehad+`, `ehad-`);
- (v) Total number of charged particles (`nch`);
- (vi) Total number of positive and negative charged particles (`nch+`, `nch-`) and their total energy (`ech+`, `ech-`);
- (vii) Total number of visible particles (`nvis`) and their total energy (`evis`);
- (viii) Total energy of the photons (`egamma`);
- (ix) *Displaced Tracks*: Particles like Λ^0 baryon ($\tau = 2.631 \times 10^{-10}$ s), K_s^0 ($\tau = 8.954 \times 10^{-11}$ s) [124] have a significant lifetime when decaying to a pair of oppositely charged daughters in case of a neutral unstable mother or a charged and neutral daughter in case of charged unstable mother would produce measurable secondary displaced tracks. The Λ_c and Λ_b^0 would also give rise to displaced tracks. The tracks are binned with their decay length ($\lambda = c\beta\gamma\tau$) mm:
 - (a) `c1`: $\lambda \in [0.3, 3.0]$,
 - (b) `c2`: $\lambda \in [3.0, 30.0]$,
 - (c) `c3`: $\lambda \in [30.0, 300.0]$,
 - (d) `c4`: $\lambda \in [300, 1200.0]$,
 - (e) `c5`: $\lambda \in [0.3, 1200.0]$, and
 - (f) `c6`: $\lambda \in [1200.0, \infty]$.
- (x) Total number of charged tracks with nonzero impact parameter (`tip`);
- (xi) A pair of charged tracks can meet at a point indicating a common mother. For such cases, we also count the number of tracks with positive and negative impact parameters separately;
- (xii) Total count of secondary displaced vertex (`sdv`) is constructed by noting a pair of charged particles coming from a displaced point from the primary vertex; and
- (xiii) The transverse mass (`mTj`) of the jet.

The above set of discrete and continuous variables are used to train our ML models. The Pearson's correlation coefficients of the variables with the jet labels ($cu \equiv 1, \bar{s}\bar{d} \equiv 0$) are shown in Table III. The table lists only those variables with more than 5% correlation with the jet class. For training ANN and BDT models, we

TABLE III. Table showing the Pearson's correlation (PC) of features with the label in $cu/\bar{s}\bar{d}$ case. The table shows only those features which have a correlation of 5% and higher.

Features	PC	Features	PC
<code>mTj</code>	-27.0	<code>c2</code>	13.7
<code>c6</code>	9.7	<code>nvis</code>	-10.0
<code>nch+</code>	-5.0	<code>nch-</code>	6.0
<code>nch</code>	10.0	<code>nlep</code>	11.4
<code>nChad</code>	-10.0	<code>nhad</code>	-11.0
<code>e1+</code>	16.0	<code>ehad</code>	-9.0

TABLE IV. The table shows the architecture of the artificial neural network used. It contains two hidden layers (Layers 1 and 2), and in each layer, a different number of nodes is used and given in column 2. The activation function used for each layer is given in the third column. We used weights as Glorot-Normal in our first hidden layer.

Layers	Nodes	Activation function	Weights
Layer 1	80	Tanh	Glorot Normal
Layer 2	40	Tanh	
Output	1	Sigmoid	

generate 10 million events, and a separate set of one million events are used for testing the models. We used Keras with TensorFlow as a backend to implement ANN, while we used XGBoost [125] to implement BDT. The parameters for BDT are chosen as follows:

- (i) Learning rate, $\eta = 0.01$;
- (ii) Maximum depth = 6;
- (iii) L2 Regularization = 1; and
- (iv) Number of gradient boosted trees = 100.

The architecture of ANN is given in Table IV. The optimization of the ANN model is done using Adam. We estimate the efficiency of the ML models by running them 1000 times on a random subset of size 60% of our test sample. The histograms of thus obtained efficiencies are shown in Fig. 4 for both ANN and BDT models. The mean value of these efficiencies is taken as our estimated efficiency of the corresponding model. We observe that the accuracy obtained using two different algorithms (ANN and BDT) overlap for three cases, i.e., u vs \bar{d} , $c\bar{s}$ vs $u\bar{d}$, cu vs $\bar{s}\bar{d}$, and for c vs \bar{s} case the two algorithm differ by $\approx 1\%$. The first two classifications are useful if one has a perfect knowledge of the event, i.e., the model making the third type of classification ($c\bar{s}$ vs $u\bar{d}$) is ideal. The ML model performs worst for the classification of u vs \bar{d} events as the final state signature obtained from the hadronization of these light quarks are nearly similar. The c vs \bar{s} event classification is fairly good with an accuracy

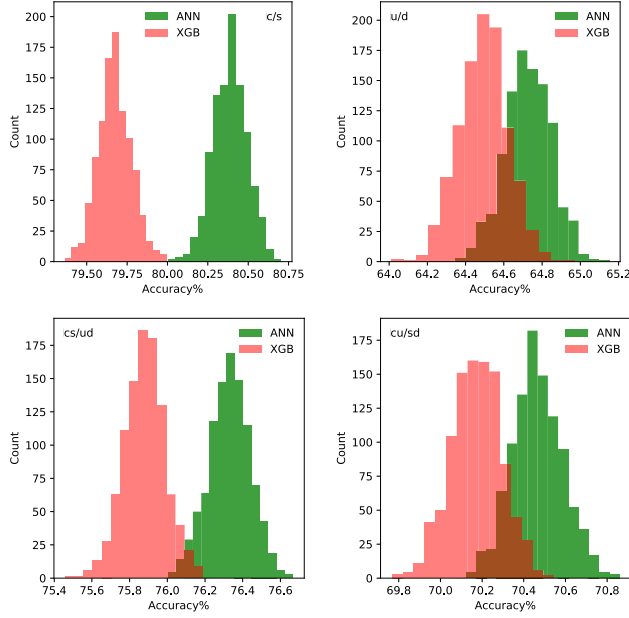


FIG. 4. Accuracy obtained using ANN and XGB for a different combination of the jet.

of $\approx 80\%$. Recent analysis performed for strange tagging in [126,127] found the efficiency to distinguish a strange jet with another jet initiated by light quarks to be $\approx 60\%$ which is lower than our result. The efficiency of our models are better since the task of classification is relatively simpler as the targeted class is either up-type or down-type in each events. For variable polarization reconstruction, it is sufficient to distinguish the up-type jets from down-type jets, i.e., cu vs $\bar{s}\bar{d}$ case. We choose the BDT algorithm for the rest of the analyses. It is to be noted that the above analysis is done using default tune of PYTHIA 8, i.e., the Monash tune [128]. The momenta and number distribution of final-state particles depend on the showering and fragmentation model and to check the robustness of our model, we train and test the models using different PYTHIA tunes. The different tunes used are `Tune::ee = 3`, `Tune::ee = 6`, `Tune::pp = 6` [129], `Tune::pp = 21` [130] and we found that the accuracy in each tunes overlaps to the Monash tune within a variance shown in Fig. 4. For further analysis, we used Monash tune.

IV. PARAMETER ESTIMATION

Apart from the cross section, we have a total of 80 asymmetries, as discussed in Sec. II. Of these, 44 are CP -even and 36 are CP -odd asymmetries. We note that the W^-W^+ production process had chiral couplings; hence the polarizations and spin-spin correlation are dependent upon the production angle θ_{W^-} . The anomalous contribution is

also $\cos \theta_{W^-}$ dependent, and using that can improve the sensitivity. We achieved this by dividing the $\cos \theta_{W^-}$ into eight bins and construct all 81 observables in each bin. This gives us a total of 648 observables. The value of observables in each bin is obtained for a set of couplings, and then those are used for numerical fitting to obtain a semianalytical expression of all the observables as a function of the couplings. For the cross section, which is a CP -even observable, the following parametrization is used to fit the data,

$$\sigma(\{c_i\}) = \sigma_0 + \sum_{i=1}^3 c^i \sigma_i + \sum_{i=1}^5 c_i^2 \sigma_{ii} + \frac{1}{2} \sum_i^3 \sum_{j(\neq i)=1}^3 c_i c_j \sigma_{ij} + c_4 c_5 \sigma_{45}. \quad (16)$$

For the asymmetries, the denominator is the cross section, and the numerator $\Delta\sigma\{c_i\} = A\{c_i\}\sigma$ is parametrized separately. For the CP -even asymmetries the parametrization of $\Delta\sigma$ is same as in Eq. (16) and for CP -odd asymmetries it is done using

$$\Delta\sigma(\{c_i\}) = \sum_{i=4}^5 c_i \sigma_i + \sum_{i=1}^3 c_i c_4 \sigma_{i4} + \sum_{i=1}^3 c_i c_5 \sigma_{i5}. \quad (17)$$

Here, c_i denotes the five couplings of the dim-6 operators $c_i = \{c_{WWW}, c_W, c_B, c_{\bar{W}}, c_{\widetilde{WWW}}\}$. We define χ^2 distance between the SM and SM plus anomalous point as

$$\chi^2(c) = \sum_k \sum_l \left(\frac{\mathcal{O}_k^l(c) - \mathcal{O}_k^l(0)}{\delta \mathcal{O}_k^l} \right)^2, \quad (18)$$

where k and l correspond to observables and bins, respectively and c denotes some nonzero anomalous couplings. The denominator $\delta \mathcal{O} = \sqrt{(\delta \mathcal{O}_{stat})^2 + (\delta \mathcal{O}_{sys})^2}$ is the estimated error in \mathcal{O} . If an observable has asymmetries $A = \frac{N^+ - N^-}{N^+ + N^-}$, the error is given by

$$\delta A = \sqrt{\frac{1 - A^2}{\mathcal{L}\sigma} + \epsilon_A^2}, \quad (19)$$

where $N^+ + N^- = N_T = \mathcal{L}\sigma$, \mathcal{L} being the integrated luminosity of the collider, which we will call luminosity for the rest of the article unless otherwise mentioned. The error in the cross section σ is given by

$$\delta\sigma = \sqrt{\frac{\sigma}{\mathcal{L}} + (\epsilon_\sigma)^2}. \quad (20)$$

Here ϵ_A and ϵ_σ are the fractional systematic error in asymmetries (A) and cross section (σ), respectively. The

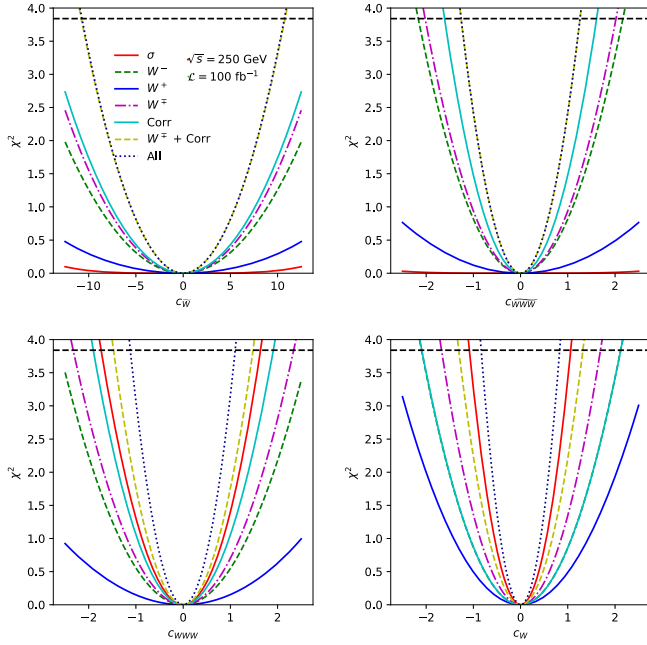


FIG. 5. χ^2 of cross section (σ), asymmetries of W boson and their combinations (W^\mp), spin-spin correlation asymmetries ($Corr$), combination of all polarization and correlation ($W^\mp + Corr$) and combination of all observables (All) as a function of anomalous couplings c_i (TeV^{-2}) one at a time. The legend is kept only for $c_{\bar{W}}$ (right panel top row) and is the same for all panels. The dashed horizontal line at $\chi^2 = 3.84$ indicates the 95% CL bound on the anomalous couplings. The systematic errors are kept to zero.

analyses in our current article is done for $\sqrt{s} = 250$ GeV and luminosity,

$$\mathcal{L} \in \{100 \text{ fb}^{-1}, 250 \text{ fb}^{-1}, 1000 \text{ fb}^{-1}, 3000 \text{ fb}^{-1}\}. \quad (21)$$

The SM cross section for the process given in Eq. (15) at $\sqrt{s} = 250$ GeV is 2.347 (pb), and with this cross section, we estimate the pure statistical error for a set of luminosity in Eq. (21) and they are

$$\frac{\delta\sigma}{\sigma} \in \{0.2\%, 0.1\%, 0.06\%, 0.03\%\}. \quad (22)$$

To the pure statistical error given above, we add a systematic error which is chosen as

$$(\epsilon_A, \epsilon_\sigma) \in \{(0, 0), (0.25\%, 0.5\%), (1\%, 2\%)\}. \quad (23)$$

We perform analyses with each value of luminosity, and for each luminosity, all systematics are chosen to give us a total of 12 different analyses.

A. One-parameter estimation

In this section, the observables are obtained by varying one anomalous coupling at a time and keeping all others to

TABLE V. The list of constraints on five anomalous couplings at 95% confidence level obtained by varying one parameter at a time and keeping the other at zero. The limits are obtained for $\sqrt{s} = 250$ GeV, luminosity $\mathcal{L} = 100 \text{ fb}^{-1}$ and 3000 fb^{-1} . The systematic errors are kept to zero.

Parameters (TeV^{-2})	100 fb^{-1}	3000 fb^{-1}
c_{WWW}/Λ^2	$[-1.12, +1.09]$	$[-0.20, +0.20]$
c_W/Λ^2	$[-0.84, +0.82]$	$[-0.15, +0.15]$
c_B/Λ^2	$[-2.65, +2.58]$	$[-0.48, +0.47]$
$c_{\bar{W}}/\Lambda^2$	$[-10.76, +10.76]$	$[-2.00, +2.00]$
$c_{\widetilde{WWW}}/\Lambda^2$	$[-1.24, +1.24]$	$[-0.22, +0.22]$

zero. We describe the role of various sets of observables in obtaining the constrain on those anomalous couplings. The systematics is kept at zero for this analyses. It is observed that the spin-spin correlation asymmetries contribute significantly to χ^2 . Together with polarization asymmetries of W 's it enhances the overall limits. In the case of CP -even couplings like c_{WWW} and c_W , the limits obtained by spin-spin correlation alone are approximately a factor of two tighter than the limits obtained using polarization asymmetries alone, see Fig. 5 bottom row. For the CP -odd couplings $c_{\bar{W}}$ and $c_{\widetilde{WWW}}$ the limits are saturated by polarization and spin-spin correlation, i.e., the cross section plays little role. This is because the cross-section in the case of CP -odd coupling behaves as

$$\sigma = \sigma_0 + c_i^2 \times \sigma_i, c_i \in \{c_{\bar{W}}, c_{\widetilde{WWW}}\}. \quad (24)$$

And for small c_i , the change in cross section is tiny. Whereas, in terms of CP -even couplings like c_{WWW} , c_W , and c_B , the cross section does provide a tighter limit on respective couplings because of linear dependence on c_i . We also note that in the case of spin-related observables, the polarization asymmetries of W^+ provide a more negligible contribution compared to that of W^- (see the green curve in Fig. 5). It is because we have reconstructed asymmetries related to W^+ using ML models, and the reconstruction is imperfect. The best limit is obtained using all the observables together. The one parameter 95% confidence level limits on various anomalous couplings c_i at $\mathcal{L} = 100 \text{ fb}^{-1}$ and 3 ab^{-1} with zero systematics are listed in Table V.

The limits on anomalous couplings c_W , c_B , and $c_{\bar{W}}$ are tighter than the experimental limits quoted in Table I. The limits on c_{WWW} and $c_{\widetilde{WWW}}$ are comparable to the best experimental limits. In comparison to the projected limits of CP -even couplings with FCC-ee [131], the limits remain comparable.

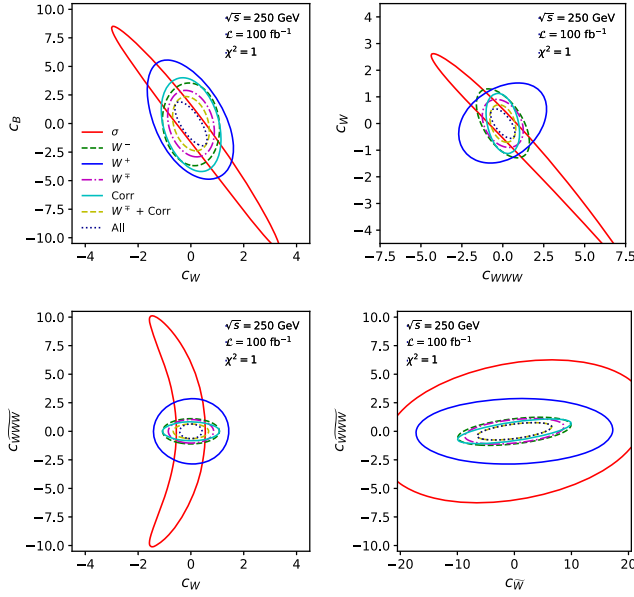


FIG. 6. Two-dimensional contour plot showing $\chi^2 = 1$ for cross section (σ), asymmetries of W boson and their combination (W^\mp), spin correlation ($Corr$), a combination of spin-related observables ($W^\mp + Corr$) and all observables (All) as a function of two anomalous couplings c_i (TeV^{-2}) at a time. The legend for each panel follows that of the right panel top row (c_W, c_B). The systematic errors are chosen to be zero.

B. Two-parameter analysis

Here we discuss the case where two out of five anomalous couplings are varied at a time, and others are kept at zero, i.e., $(c_i, c_j)_{i \neq j}, c_i, c_j \in (c_{WWW}, c_W, c_B, c_{\bar{W}}, c_{\widetilde{WWW}})$. We study how various sets of observables perform on constraining pairs of anomalous couplings. Each observable corresponding to individual pair (c_i, c_j) is fitted to Eqs. (16) and (17) and the fitted function are used to compute χ^2 using Eq. (18). We kept the systematic error at zero for this analysis. In Fig. 6, we show four different pairs depicting $\chi^2 = 1$ contour from a total of $\binom{5}{2} = 10$ pairs. It is observed that only certain combinations are correlated like $\{(c_W, c_B), (c_{WWW}, c_W), (c_{\bar{W}}, c_{\widetilde{WWW}})\}$ and the other remaining pairs shows little or no correlations. The contribution of various observables on constraining the anomalous couplings is shown in various panels of Fig. 6. The behavior of red contours due to cross section σ can be understood as follows. In terms of two parameters σ behaves as

$$\sigma = \sigma_0 + c_1\sigma_{01} + c_2\sigma_{02} + c_1^2\sigma_{11} + c_2^2\sigma_{22} + c_{12}\sigma_{12}. \quad (25)$$

In the bottom right panel of Fig. 6, both the parameters are CP -odd, i.e., the linear terms in the above equation are absent, as was observed in the previous section. This leads to a poor constraint on both parameters; hence, the

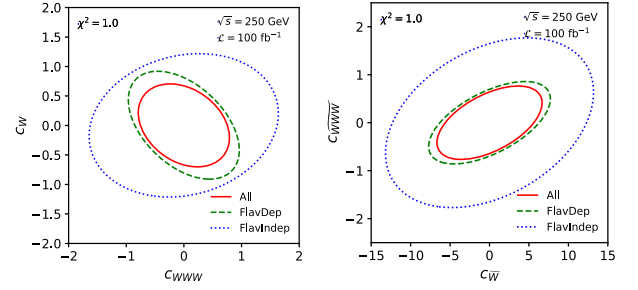


FIG. 7. $\chi^2 = 1$ contour for combinations of all asymmetries, flavor-dependent, and flavor-independent asymmetries as a function of two anomalous couplings c_i (TeV^{-2}) at a time. The results is obtained for $\sqrt{s} = 250$ GeV, $\mathcal{L} = 100$ fb $^{-1}$, and zero systematics.

corresponding contour is large. In the top row, both the parameters are CP -even, and hence all terms of Eq. (25) are nonzero. The contribution from the quadratic pieces, i.e., the last two terms, is always positive. The contribution from the linear can be of either sign depending upon the sign of the couplings and the sign of the interference terms σ_{01} and σ_{02} . They lead to a vanishing contribution along the line

$$c_1\sigma_{01} + c_2\sigma_{02} = 0 \quad \text{or} \quad c_1 = -c_2 \frac{\sigma_{02}}{\sigma_{01}}.$$

As it is clear from the figure, σ_{01} and σ_{02} are of the same sign and hence a poor limit along the above line in the second and fourth quadrants. The same leads to a tighter constraint in the orthogonal direction. In the case of pair containing CP -even and CP -odd parameters, the cross section as defined in Eq. (25) contains only one linear term coming from CP -even parameter, thus we see tight constraints on the x -axis (CP -even) and loose constraints on the y -axis (CP -odd). The asymmetries are rational polynomials of the second degree and can have complicated shapes depending upon their CP nature and the pair of couplings we are probing. The contours from the W^+ polarization alone are wider than the one obtained from W^- as in one-parameter analyses. The contours due to correlations alone are comparable to the contribution of other observables. A combination is expected to improve the constraint.

At this juncture, it is essential to question the importance of flavor tagging. To do that, we show how the contour changes with different asymmetries, viz. flavor dependent, flavor independent, and their combinations as a function of anomalous couplings. The $\chi^2 = 1$ contour plots for (c_{WWW}, c_W) and $(c_{\bar{W}}, c_{\widetilde{WWW}})$ are shown in the right and left panel of Fig. 7 respectively. In both the panel, it is clear that even with 70% accuracy on flavor tagging, the dominant contribution on constraining the anomalous couplings comes from the flavor-dependent observables.

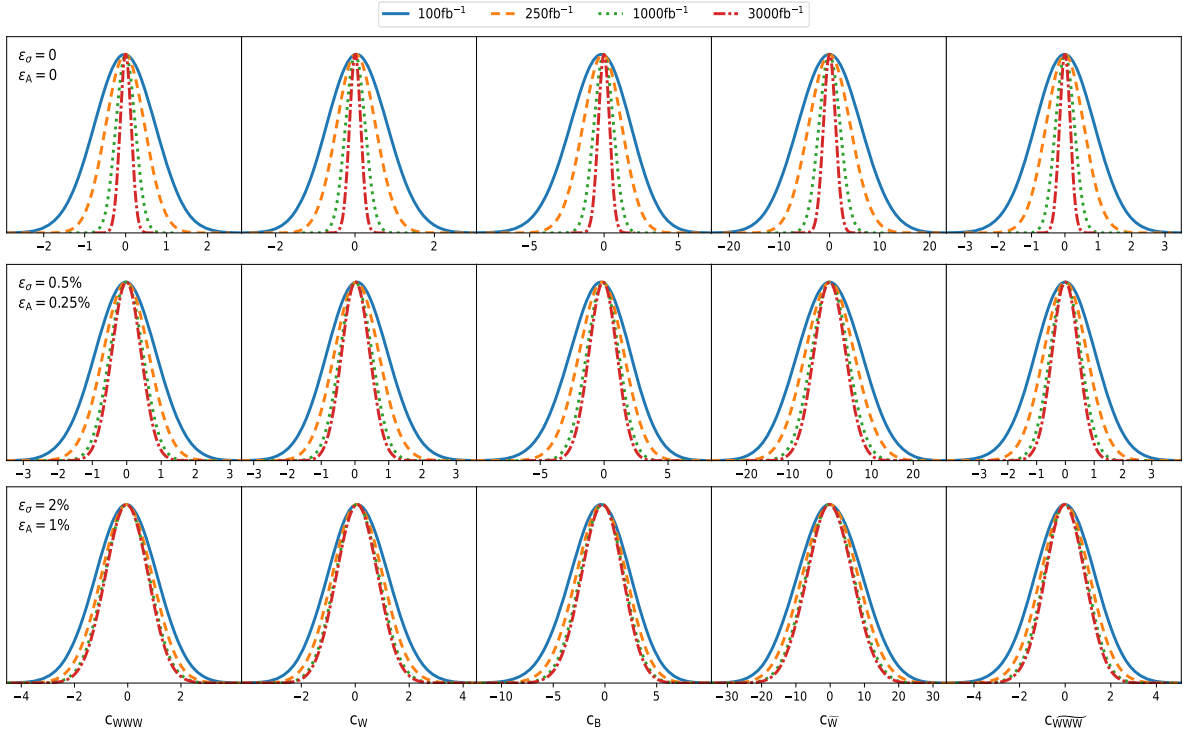


FIG. 8. Marginalized 1D projections at 95% CL from the MCMC for the effective operators c_i (TeV^{-2}) for a set of systematic error and luminosities. The value of the systematics used is given in the first plots of each row.

This suggests that we need to develop a higher-accuracy model. For further analyses, we consider all the observables (cross section and asymmetries).

C. Five-parameter analysis

Next, we move to a full 5-dimensional parameter space, where all parameters can vary simultaneously. We also did five parameters fitting as in Eqs. (16) and (17). We used the fitted function to perform Markov Chain Monte Carlo (MCMC) [124] analyses to estimate simultaneous limits on the anomalous couplings. MCMC is essentially Monte Carlo integration using Markov chains. This kind of integration is usually used over the high-dimensional probability distributions to make inferences about model parameters or to make predictions. The chain can be constructed following the general algorithm suggested by Metropolis and Hastings [132,133]. If \mathcal{O} denotes the observed data and θ denotes model parameters; we can set up joint probability distribution $P(\mathcal{O}, \theta)$ over all random quantities which can be defined as

$$P(\mathcal{O}, \theta) = P(\mathcal{O}|\theta)P(\theta), \quad (26)$$

where $P(\theta)$ and $P(\mathcal{O}|\theta)$ are prior and likelihood distribution, respectively. Bayes theorem can be used to find the posterior distribution of θ ,

$$P(\theta|\mathcal{O}) = \frac{P(\theta)P(\mathcal{O}|\theta)}{\int P(\theta)P(\mathcal{O}|\theta)d\theta}. \quad (27)$$

Any features of the posterior distribution can be expressed in terms of posterior expectations of functions of θ given by

$$E[f(\theta)|\mathcal{O}] = \frac{\int f(\theta)P(\theta)P(\mathcal{O}|\theta)d\theta}{\int P(\theta)P(\mathcal{O}|\theta)d\theta}. \quad (28)$$

Our current analysis has five different parameters (c_i) and 648 observables, as already described. We defined a likelihood function by using the χ^2 defined in Eq. (18) and is defined as

$$P(c_i|\mathcal{O}) \propto e^{-\frac{\chi^2(c_i)}{2}}. \quad (29)$$

The further interpretation of the posterior probability to find the Bayesian confidence interval is made using GetDist [134]. It is a Python package for analyzing Monte Carlo samples, including correlated samples from MCMC. The samples are obtained for a set of luminosities \mathcal{L} with different combinations of systematic error of cross section and asymmetries. For each combination of luminosity and systematic error, we generated 50 chains of samples initiated with different values of parameters. We begin by observing marginalized 1d projections at 95%

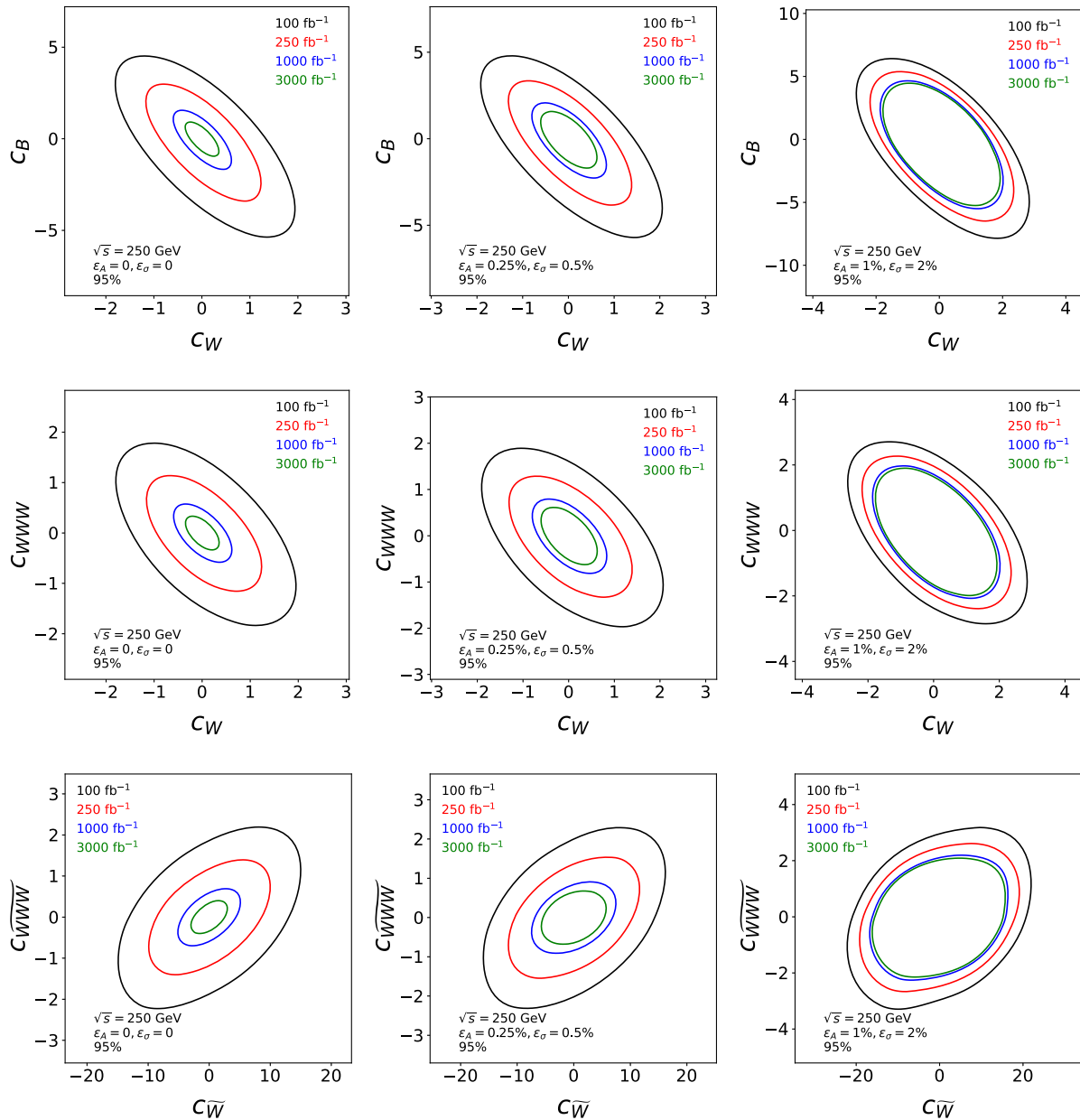


FIG. 9. Marginalized 2D projections of the maximally correlated anomalous couplings c_i (TeV^{-2}) at 95% CL from the MCMC for a set of systematic error and luminosities obtained using GetDist at the *reconstruction level*.

confidence level (see Fig. 8) obtained using MCMC at different luminosities and systematics. We observed (top row of Fig. 8) that when systematics is chosen to be $(0,0)$, the confidence interval on anomalous couplings (c_i) tightens on increasing luminosity \mathcal{L} . The limits vary as $\approx \frac{1}{\sqrt{\mathcal{L}}}$. And when the systematics is chosen at $(0.25\%, 0.5\%)$ for asymmetries and cross sections, respectively, we note (middle row of Fig. 8) the confidence interval tightens with increasing luminosity $\mathcal{L} \in [100 \text{ fb}^{-1}, 1000 \text{ fb}^{-1}]$ and the limits on every anomalous couplings saturates above

1000 fb^{-1} . The bottom row of Fig. 8 represents the variations of the confidence interval of various anomalous couplings when the systematics are kept at $(1\%, 2\%)$ and it is observed that the limits saturate at luminosity $\mathcal{L} = 250 \text{ fb}^{-1}$. Similar arguments can be made by observing Fig. 9, which is a marginalized 2d projection of the correlated parameters at 95% confidence level. Other combinations of parameters are found to be minimally correlated or uncorrelated. The plots are shown for three sets of systematic errors at different luminosities. The left,

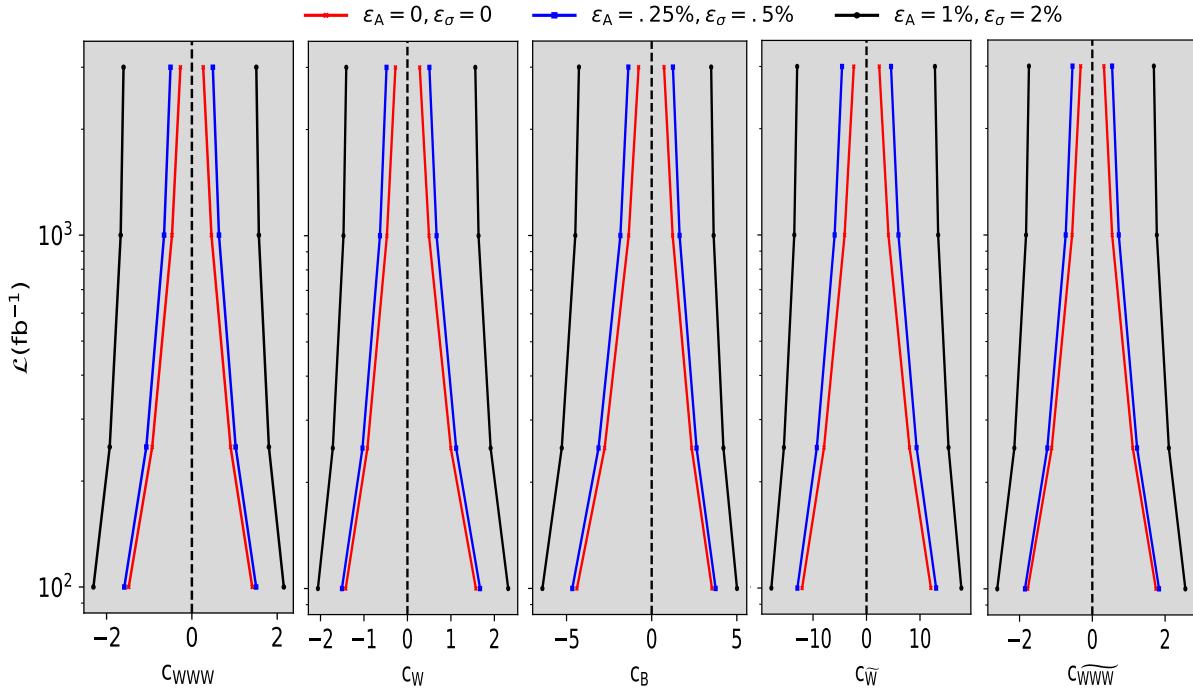


FIG. 10. The variation of the values of the five anomalous couplings c_i (TeV^{-2}) with respect to luminosities \mathcal{L} at different value of systematic error $(\epsilon_A, \epsilon_\sigma)$.

middle, and right panel of each row of Fig. 9 represent when systematics are chosen to be $(0,0)$, $(0.25\%, 0.5\%)$, and $(1\%, 2\%)$, respectively. As one moves from the left to the right panel (increasing systematic error) in each row, the simultaneous limits on two anomalous couplings get saturated at a certain luminosity. As can be noted from the middle and right panel of Fig. 9, the simultaneous limits on two parameters saturate around 1000 fb^{-1} and 250 fb^{-1} , respectively. Finally, we show in Fig. 10 the variation of limits of all five anomalous couplings with respect to \mathcal{L} at fix ϵ_A and ϵ_σ . It depicts how the limits of different couplings vary with respect to luminosities at a fixed systematic error.

TABLE VI. The list of 95% BCI of anomalous couplings (TeV^{-2}) of effective operators for $\sqrt{s} = 250 \text{ GeV}$ and $\mathcal{L} \in \{100 \text{ fb}^{-1}, 250 \text{ fb}^{-1}, 1000 \text{ fb}^{-1}, 3000 \text{ fb}^{-1}\}$ at systematic error of $(\epsilon_A, \epsilon_\sigma) = (1\%, 2\%)$ from MCMC global fits at the reconstruction level. The reconstruction of W^+ is done using XGBoost.

Parameters	100 fb^{-1}	250 fb^{-1}	1000 fb^{-1}	3000 fb^{-1}
$\frac{c_{WWW}}{\Lambda^2}$	+2.1 -2.3	+1.8 -1.9	+1.6 -1.7	+1.5 -1.5
$\frac{c_W}{\Lambda^2}$	+2.3 -2.0	+1.9 -1.7	+1.6 -1.5	+1.6 -1.4
$\frac{c_B}{\Lambda^2}$	+5.0 -6.4	+4.2 -5.3	+3.6 -4.5	+3.5 -4.3
$\frac{c_{\tilde{W}}}{\Lambda^2}$	+17.7 -17.8	+15.3 -15.4	+13.4 -13.5	+12.8 -13.0
$\frac{c_{\widetilde{WWW}}}{\Lambda^2}$	+2.6 -2.6	+2.1 -2.1	+1.8 -1.8	+1.7 -1.7

As can be seen in Fig. 10, the limits at systematics of $(1\%, 2\%)$ for asymmetries and cross section, respectively, shown by black curve saturates, suggesting that the best limits set on various couplings do not improve with luminosity. It can be further noted that the limit set at chosen maximal luminosity (3000 fb^{-1}) and maximal systematics $(1\%, 2\%)$ is still worse than when we chose minimal luminosity (100 fb^{-1}) but reduced systematics $(0.25\%, 0.5\%)$. For example, we take c_{WWW} , the limit at $(\epsilon_A, \epsilon_\sigma) = (1\%, 2\%)$ and $\mathcal{L} = 100 \text{ fb}^{-1}$ is approximately $[-2.2, +2.2]$ and these limit becomes approximately $[-2.0, +2.0]$ at a luminosity value of 3000 fb^{-1} . The latter value can be achieved if we choose the systematics to be $(0.25\%, 0.5\%)$ and luminosity is kept at 100 fb^{-1} . All the other anomalous couplings show the same behavior. These suggest that increasing the luminosity would not be very advantageous unless the systematic error is not brought down to a sizeable value. The limit for different parameters (c_i) at 95% confidence interval for $(\epsilon_A, \epsilon_\sigma) = (1\%, 2\%)$ are noted down in Table VI. We found that the limits set by our analyses on the parameters like c_B and $c_{\tilde{W}}$ are tighter than that of the quoted experimental value in Table I while the limits on other anomalous couplings ($c_{WWW}, c_W, c_{\widetilde{WWW}}$) remains comparable. The limits on $c_{\tilde{W}}$ improve by a factor of ≈ 1.18 , and for c_B , the limit shrinks by a factor of ≈ 1.7 . We further note that the limit obtained in this article for

anomalous couplings like c_W and c_B are tighter by a factor of ≈ 1.5 and 2.3 , respectively, than those obtained by [11]. The limits by [11] were obtained at $\sqrt{s} = 500$ GeV at the level of parton, i.e., there was no error in the reconstruction of W^+ boson.

V. CONCLUSION

In this article, we use machine learning techniques like artificial neural networks and boosted decision trees to tag the jets initiated by light flavor quarks with about 70% accuracy. The classification is made on two classes defined as up-type or down-type jets. The reconstructed W^+ remains a faithful object for constructing all the observables we have used in this work to constrain the anomalous couplings. It is always an advantage to have as many observables as possible to probe or measure various parameters of new physics. We have shown that spin-spin correlation asymmetries can provide constraints comparable to those of polarization asymmetries. We also exploit the fact that the spin and polarization asymmetries vary with the production angle θ_{W^-} by dividing the $\cos \theta_{W^-}$ into eight equal bins and constructing all 80 asymmetries in all those bins. This and the cross sections in those bins give us a total of 648 observables that depend upon the five anomalous couplings.

Our one parameter limits shown in Table V for $\mathcal{L} = 100 \text{ fb}^{-1}$ are better than the one parameter limits in Table I obtained from various analyses [48,49,57] at CMS. Our five parameter simultaneous limits in Table VI for $\mathcal{L} = 100 \text{ fb}^{-1}$ are also comparable to the one parameter limits in Table I for c_W , c_B , and $c_{\tilde{W}}$. While for c_{WWW} and $c_{\widetilde{WWW}}$, the CMS limits obtained using production rates alone are better than what we quote. This is because the contributions proportional to c_{WWW} and $c_{\widetilde{WWW}}$ have an extra factor of p^2 in the matrix element, which leads to an enhanced contribution in machinelike LHC running at 13 TeV. In our case, the limit $c_{\widetilde{WWW}}$ is derived mainly from the asymmetries and without the advantage of large momentum. For c_{WWW} , however, the cross section provides a strong limit (Fig. 5), but there is some cancellation in the cross section due to nonzero values of c_W and c_B (Fig. 6) which leads to a poorer limit than Table V when all parameters are varied.

We showed how systematic error act as a brick in constraining anomalous couplings. For example, for a conservative choice of systematics to be $(\epsilon_A, \epsilon_\sigma) = (1\%, 2\%)$, the limits on the anomalous couplings improve by a factor of only ~ 1.4 when we increase the luminosity from 100 fb^{-1} to 3000 fb^{-1} . This indicates that with large systematics, it is wise to look for additional observables from various processes to constrain the couplings better than to run the machine for a higher luminosity. One can also try to improve the flavor tagging, use the beam polarization, and use a finer binning of the production angle $\cos \theta_{W^-}$ while running the machine at $\sqrt{s} = 250$ GeV.

ACKNOWLEDGMENTS

We thank Rafiqul Rahaman for the useful discussions. A. S thanks CSIR-UGC, Government of India, for financial support.

APPENDIX: NORMALIZED POLARIZATION AND DECAY DENSITY MATRIX

The polarization density matrix for a spin-1 particle is given as $\rho(\lambda, \lambda') =$

$$\begin{bmatrix} \frac{1}{3} + \frac{p_z}{2} + \frac{T_{zz}}{\sqrt{6}} & \frac{p_x - ip_y}{2\sqrt{2}} + \frac{T_{xz} - iT_{yz}}{\sqrt{3}} & \frac{T_{xz} - T_{yy} - iT_{xy}}{\sqrt{6}} \\ \frac{p_x + ip_y}{2\sqrt{2}} + \frac{T_{xz} + iT_{yz}}{\sqrt{3}} & \frac{1}{3} - \frac{2T_{zz}}{\sqrt{6}} & \frac{p_x - ip_y}{2\sqrt{2}} - \frac{T_{xz} - iT_{yz}}{\sqrt{3}} \\ \frac{T_{xx} - T_{yy} + 2iT_{xy}}{\sqrt{6}} & \frac{p_x + ip_y}{2\sqrt{2}} - \frac{T_{xz} + iT_{yz}}{\sqrt{3}} & \frac{1}{3} - \frac{p_z}{2} + \frac{T_{zz}}{\sqrt{6}} \end{bmatrix}, \quad (\text{A1})$$

and the normalized decay density matrix $\Gamma(\lambda, \lambda') =$

$$\begin{bmatrix} \frac{1 + \delta + \rho c_\theta^2 + 2\alpha s_\theta}{4} & \frac{s_\theta + d\delta c_\theta}{2\sqrt{2}} e^{i\phi} & \rho \frac{(1 - c_\theta^2)}{4} e^{i2\phi} \\ \frac{s_\theta(\alpha + \rho c_\theta)}{2\sqrt{2}} e^{-i\phi} & \delta + \rho \frac{s_\theta^2}{2} & \frac{s_\theta(\alpha - \rho c_\theta)}{2\sqrt{2}} e^{i\phi} \\ \rho \frac{(1 - c_\theta^2)}{4} e^{-i2\phi} & \frac{s_\theta(\alpha - \rho c_\theta)}{2\sqrt{2}} e^{-i\phi} & \frac{1 + \delta + \rho c_\theta^2 - 2\alpha c_\theta}{4} \end{bmatrix}, \quad (\text{A2})$$

where c_θ and s_θ are $\cos \theta$ and $\sin \theta$ of the polar angle of the decay products respectively and $\rho = (1 - 3\delta)$.

- [1] S. Chatrchyan *et al.* (CMS Collaboration), Observation of a new boson at a mass of 125 GeV with the CMS experiment at the LHC, *Phys. Lett. B* **716**, 30 (2012).
- [2] G. Aad *et al.* (ATLAS Collaboration), Observation of a new particle in the search for the Standard Model Higgs boson with the ATLAS detector at the LHC, *Phys. Lett. B* **716**, 1 (2012).
- [3] P. A. R. Ade *et al.* (Planck Collaboration), Planck 2013 results. XVI. Cosmological parameters, *Astron. Astrophys.* **571**, A16 (2014).
- [4] T. Aaltonen *et al.* (CDF Collaboration), High-precision measurement of the W boson mass with the CDF II detector, *Science* **376**, 170 (2022).
- [5] B. Abi *et al.* (Muon $g - 2$ Collaboration), Measurement of the Positive Muon Anomalous Magnetic Moment to 0.46 ppm, *Phys. Rev. Lett.* **126**, 141801 (2021).
- [6] W. Buchmuller and D. Wyler, Effective Lagrangian analysis of new interactions and flavor conservation, *Nucl. Phys.* **B268**, 621 (1986).
- [7] K. Hagiwara, S. Ishihara, R. Szalapski, and D. Zeppenfeld, Low energy effects of new interactions in the electroweak boson sector, *Phys. Rev. D* **48**, 2182 (1993).
- [8] C. Degrande, N. Greiner, W. Kilian, O. Mattelaer, H. Mebane, T. Stelzer, S. Willenbrock, and C. Zhang, Effective field theory: A modern approach to anomalous couplings, *Ann. Phys. (Amsterdam)* **335**, 21 (2013).
- [9] K. Hagiwara, R. D. Peccei, D. Zeppenfeld, and K. Hikasa, Probing the weak boson sector in $e^+e^- \rightarrow W^+W^-$, *Nucl. Phys.* **B282**, 253 (1987).
- [10] Z. Zhang, Time to Go Beyond Triple-Gauge-Boson-Coupling Interpretation of W Pair Production, *Phys. Rev. Lett.* **118**, 011803 (2017).
- [11] R. Rahaman and R. K. Singh, Probing the anomalous triple gauge boson couplings in $e^+e^- \rightarrow W^+W^-$ using W polarizations with polarized beams, *Phys. Rev. D* **101**, 075044 (2020).
- [12] C. L. Bilchak and J. D. Stroughair, W^+W^- pair production in e^+e^- colliders, *Phys. Rev. D* **30**, 1881 (1984).
- [13] K. J. F. Gaemers and G. J. Gounaris, Polarization amplitudes for $e^+e^- \rightarrow W^+W^-$ and $e^+e^- \rightarrow ZZ$, *Z. Phys. C* **1**, 259 (1979).
- [14] K. Hagiwara, S. Ishihara, R. Szalapski, and D. Zeppenfeld, Low-energy constraints on electroweak three gauge boson couplings, *Phys. Lett. B* **283**, 353 (1992).
- [15] D. Choudhury and J. Kalinowski, Unraveling the $WW\gamma$ and WWZ vertices at the linear collider: Anti-neutrino neutrino γ and anti-neutrino neutrino $\bar{q}q$ final states, *Nucl. Phys.* **B491**, 129 (1997).
- [16] D. Choudhury, J. Kalinowski, and A. Kulesza, CP violating anomalous $WW\gamma$ couplings in e^+e^- collisions, *Phys. Lett. B* **457**, 193 (1999).
- [17] J. D. Wells and Z. Zhang, Status and prospects of precision analyses with $e^+e^- \rightarrow W^+W^-$, *Phys. Rev. D* **93**, 034001 (2016).
- [18] G. Buchalla, O. Cata, R. Rahn, and M. Schlaffer, Effective field theory analysis of new physics in $e^+e^- \rightarrow W^+W^-$ at a linear collider, *Eur. Phys. J. C* **73**, 2589 (2013).
- [19] L. Berthier, M. Bjørn, and M. Trott, Incorporating doubly resonant W^\pm data in a global fit of SMEFT parameters to lift flat directions, *J. High Energy Phys.* **09** (2016) 157.
- [20] L. Bian, J. Shu, and Y. Zhang, Triple gauge couplings at future hadron and lepton colliders, *Int. J. Mod. Phys. A* **31**, 1644008 (2016).
- [21] J. Beyer, R. Karl, and J. List, Precision measurements of triple gauge couplings at future electron-positron colliders, in *International Workshop on Future Linear Colliders* (2020), arXiv:2002.02777.
- [22] L. Bian, J. Shu, and Y. Zhang, Prospects for triple gauge coupling measurements at future lepton colliders and the 14 TeV LHC, *J. High Energy Phys.* **09** (2015) 206.
- [23] J. Baglio, S. Dawson, and S. Homiller, QCD corrections in Standard Model EFT fits to WZ and WW production, *Phys. Rev. D* **100**, 113010 (2019).
- [24] D. Choudhury, K. Deka, S. Maharana, and L. K. Saini, Anomalous gauge couplings vis-à-vis $(g - 2)_\mu$ and flavor observables, *Phys. Rev. D* **106**, 115026 (2022).
- [25] U. Baur and D. Zeppenfeld, Unitarity constraints on the electroweak three vector boson vertices, *Phys. Lett. B* **201**, 383 (1988).
- [26] A. Butter, O. J. P. Éboli, J. Gonzalez-Fraile, M. C. Gonzalez-Garcia, T. Plehn, and M. Rauch, The gauge-Higgs legacy of the LHC run I, *J. High Energy Phys.* **07** (2016) 152.
- [27] A. Azatov, J. Elias-Miro, Y. Reyimuaji, and E. Venturini, Novel measurements of anomalous triple gauge couplings for the LHC, *J. High Energy Phys.* **10** (2017) 027.
- [28] H. T. Li and G. Valencia, CP violating anomalous couplings in W jet production at the LHC, *Phys. Rev. D* **96**, 075014 (2017).
- [29] J. Baglio, S. Dawson, and I. M. Lewis, NLO QCD effective field theory analysis of W^+W^- production at the LHC including fermionic operators, *Phys. Rev. D* **96**, 073003 (2017).
- [30] D. Bhatia, U. Maitra, and S. Raychaudhuri, Pinning down anomalous $WW\gamma$ couplings at the LHC, *Phys. Rev. D* **99**, 095017 (2019).
- [31] M. Chiesa, A. Denner, and J.-N. Lang, Anomalous triple-gauge-boson interactions in vector-boson pair production with RECOLA2, *Eur. Phys. J. C* **78**, 467 (2018).
- [32] R. Rahaman and R. K. Singh, Unravelling the anomalous gauge boson couplings in ZW^\pm production at the LHC and the role of spin-1 polarizations, *J. High Energy Phys.* **04** (2020) 075.
- [33] S. Tizchang and S. M. Etesami, Pinning down the gauge boson couplings in $WW\gamma$ production using forward proton tagging, *J. High Energy Phys.* **07** (2020) 191.
- [34] F. Campanario, M. Kerner, N. D. Le, and I. Rosario, Diphoton production in vector-boson scattering at the LHC at next-to-leading order QCD, *J. High Energy Phys.* **06** (2020) 072.
- [35] V. Ciulli (CMS Collaboration), Electroweak measurements with the CMS detector, *Acta Phys. Pol. B* **51**, 1315 (2020).
- [36] J. Baglio, S. Dawson, and I. M. Lewis, An NLO QCD effective field theory analysis of W^+W^- production at the LHC including fermionic operators, *Phys. Rev. D* **96**, 073003 (2017).
- [37] S. S. Biswal, M. Patra, and S. Raychaudhuri, Anomalous triple gauge vertices at the large hadron-electron collider, arXiv:1405.6056.

- [38] I. T. Cakir, O. Cakir, A. Senol, and A. T. Tasci, Search for anomalous $WW\gamma$ and WWZ couplings with polarized e -beam at the LHeC, *Acta Phys. Pol. B* **45**, 1947 (2014).
- [39] R. Li, X.-M. Shen, K. Wang, T. Xu, L. Zhang, and G. Zhu, Probing anomalous $WW\gamma$ triple gauge bosons coupling at the LHeC, *Phys. Rev. D* **97**, 075043 (2018).
- [40] M. Köksal, A. A. Billur, A. Gutiérrez-Rodríguez, and M. A. Hernández-Ruiz, Bounds on the non-standard $W^+W^-\gamma$ couplings at the LHeC and the FCC-he, *Phys. Lett. B* **808**, 135661 (2020).
- [41] A. Gutiérrez-Rodríguez, M. Köksal, A. A. Billur, and M. A. Hernández-Ruiz, Probing model-independent limits on $W^+W^-\gamma$ triple gauge boson vertex at the LHeC and the FCC-he, *J. Phys. G* **47**, 055005 (2020).
- [42] G. Abbiendi *et al.* (OPAL Collaboration), Measurement of W boson polarizations and CP violating triple gauge couplings from W^+W^- production at LEP, *Eur. Phys. J. C* **19**, 229 (2001).
- [43] OPAL Collaboration, Measurement of charged current triple gauge boson couplings using W pairs at LEP, *Eur. Phys. J. C* **33**, 463 (2004).
- [44] J. Abdallah *et al.* (DELPHI Collaboration), Study of W boson polarisations and triple gauge boson couplings in the reaction $e^+e^- \rightarrow W^+W^-$ at LEP 2, *Eur. Phys. J. C* **54**, 345 (2008).
- [45] S. Schael *et al.* (ALEPH, DELPHI, L3, OPAL, and LEP Electroweak Collaborations), Electroweak measurements in electron-positron collisions at W -boson-pair energies at LEP, *Phys. Rep.* **532**, 119 (2013).
- [46] L. J. Dixon, Z. Kunszt, and A. Signer, Vector boson pair production in hadronic collisions at order α_s : Lepton correlations and anomalous couplings, *Phys. Rev. D* **60**, 114037 (1999).
- [47] A. Falkowski, M. Gonzalez-Alonso, A. Greljo, D. Marzocca, and M. Son, Anomalous triple gauge couplings in the effective field theory approach at the LHC, *J. High Energy Phys.* **02** (2017) 115.
- [48] A. Tumasyan *et al.* (CMS Collaboration), Measurement of the inclusive and differential WZ production cross sections, polarization angles, and triple gauge couplings in pp collisions at $\sqrt{s} = 13$ TeV, *J. High Energy Phys.* **07** (2022) 032.
- [49] A. M. Sirunyan *et al.* (CMS Collaboration), Measurement of the $W\gamma$ Production Cross Section in Proton-Proton Collisions at $\sqrt{s} = 13$ TeV and Constraints on Effective Field Theory Coefficients, *Phys. Rev. Lett.* **126**, 252002 (2021).
- [50] A. Tumasyan *et al.*, Measurement of the inclusive and differential WZ production cross sections, polarization angles, and triple gauge couplings in pp collisions at $\sqrt{s} = 13$ TeV, *J. High Energy Phys.* **07** (2022) 032.
- [51] V. Khachatryan *et al.* (CMS Collaboration), Measurement of the WZ production cross section in pp collisions at $\sqrt{s} = 7$ and 8 TeV and search for anomalous triple gauge couplings at $\sqrt{s} = 8$ TeV, *Eur. Phys. J. C* **77**, 236 (2017).
- [52] S. Chatrchyan *et al.* (CMS Collaboration), Measurement of the W^+W^- cross section in pp collisions at $\sqrt{s} = 7$ TeV and limits on anomalous $WW\gamma$ and WWZ couplings, *Eur. Phys. J. C* **73**, 2610 (2013).
- [53] S. Chatrchyan *et al.* (CMS Collaboration), Measurement of the sum of WW and WZ production with $W +$ Dijet events in pp collisions at $\sqrt{s} = 7$ TeV, *Eur. Phys. J. C* **73**, 2283 (2013).
- [54] S. Chatrchyan *et al.* (CMS Collaboration), Measurement of the $W\gamma$ and $Z\gamma$ inclusive cross sections in pp collisions at $\sqrt{s} = 7$ TeV and limits on anomalous triple gauge boson couplings, *Phys. Rev. D* **89**, 092005 (2014).
- [55] A. M. Sirunyan *et al.* (CMS Collaboration), Search for anomalous couplings in boosted $WW/WZ \rightarrow \ell\nu q\bar{q}$ production in proton-proton collisions at $\sqrt{s} = 8$ TeV, *Phys. Lett. B* **772**, 21 (2017).
- [56] A. M. Sirunyan *et al.* (CMS Collaboration), Electroweak production of two jets in association with a Z boson in proton-proton collisions at $\sqrt{s} = 13$ TeV, *Eur. Phys. J. C* **78**, 589 (2018).
- [57] A. M. Sirunyan *et al.* (CMS Collaboration), Search for anomalous triple gauge couplings in WW and WZ production in lepton + jet events in proton-proton collisions at $\sqrt{s} = 13$ TeV, *J. High Energy Phys.* **12** (2019) 062.
- [58] A. M. Sirunyan *et al.* (CMS Collaboration), Measurement of electroweak production of a W boson in association with two jets in proton-proton collisions at $\sqrt{s} = 13$ TeV, *Eur. Phys. J. C* **80**, 43 (2020).
- [59] A. M. Sirunyan *et al.* (CMS Collaboration), Measurements of the $pp \rightarrow WZ$ inclusive and differential production cross section and constraints on charged anomalous triple gauge couplings at $\sqrt{s} = 13$ TeV, *J. High Energy Phys.* **04** (2019) 122.
- [60] P. Rebello Teles (CMS Collaboration), Search for anomalous gauge couplings in semi-leptonic decays of $WW\gamma$ and $WZ\gamma$ in pp collisions at $\sqrt{s} = 8$ TeV, in *Meeting of the APS Division of Particles and Fields* (2013), arXiv:1310.0473.
- [61] G. Aad *et al.* (ATLAS Collaboration), Measurements of $W^+W^- + \geq 1$ jet production cross-sections in pp collisions at $\sqrt{s} = 13$ TeV with the ATLAS detector, *J. High Energy Phys.* **06** (2021) 003.
- [62] G. Aad *et al.* (ATLAS Collaboration), Measurements of $W^{\pm Z}$ production cross sections in pp collisions at $\sqrt{s} = 8$ TeV with the ATLAS detector and limits on anomalous gauge boson self-couplings, *Phys. Rev. D* **93**, 092004 (2016).
- [63] G. Aad *et al.* (ATLAS Collaboration), Measurement of total and differential W^+W^- production cross sections in proton-proton collisions at $\sqrt{s} = 8$ TeV with the ATLAS detector and limits on anomalous triple-gauge-boson couplings, *J. High Energy Phys.* **09** (2016) 029.
- [64] G. Aad *et al.* (ATLAS Collaboration), Measurement of W^+W^- production in pp collisions at $\sqrt{s} = 7$ TeV with the ATLAS detector and limits on anomalous WWZ and $WW\gamma$ couplings, *Phys. Rev. D* **87**, 112001 (2013); G. Aad (ATLAS Collaboration), *Phys. Rev. D* **88**, 079906(E) (2013).
- [65] G. Aad *et al.* (ATLAS Collaboration), Measurements of $W\gamma$ and $Z\gamma$ production in pp collisions at $\sqrt{s} = 7$ TeV with the ATLAS detector at the LHC, *Phys. Rev. D* **87**, 112003 (2013); **91**, 119901(E) (2015).
- [66] M. Aaboud *et al.* (ATLAS Collaboration), Measurement of $WW/WZ \rightarrow \ell\nu q\bar{q}'$ production with the hadronically

- decaying boson reconstructed as one or two jets in pp collisions at $\sqrt{s} = 8$ TeV with ATLAS, and constraints on anomalous gauge couplings, *Eur. Phys. J. C* **77**, 563 (2017).
- [67] M. Aaboud *et al.* (ATLAS Collaboration), Measurements of electroweak Wjj production and constraints on anomalous gauge couplings with the ATLAS detector, *Eur. Phys. J. C* **77**, 474 (2017).
- [68] Y.C. Yap, Recent observation and measurements of diboson processes from the ATLAS experiment, *Mod. Phys. Lett. A* **35**, 2030013 (2020).
- [69] T. Aaltonen *et al.* (CDF Collaboration), Limits on anomalous triple gauge couplings in $p\bar{p}$ collisions at $\sqrt{s} = 1.96$ -TeV, *Phys. Rev. D* **76**, 111103 (2007).
- [70] T. Aaltonen *et al.* (CDF Collaboration), Measurement of the WZ cross section and triple gauge couplings in $p\bar{p}$ collisions at $\sqrt{s} = 1.96$ TeV, *Phys. Rev. D* **86**, 031104 (2012).
- [71] V.M. Abazov *et al.* (D0 Collaboration), Measurement of the $WZ \rightarrow \ell\nu\ell\ell$ cross section and limits on anomalous triple gauge couplings in $p\bar{p}$ collisions at $\sqrt{s} = 1.96$ TeV, *Phys. Lett. B* **695**, 67 (2011).
- [72] D. Krop (CDF and D0 Collaborations), Search for new physics with photons and exclusive Z production at the tevatron, in *International Conference on the Structure and Interactions of the Photon and 18th International Workshop on Photon-Photon Collisions and International Workshop on High Energy Photon Linear Colliders* (2010), pp. 3–10, [10.3204/DESY-PROC-2009-03/Krop](https://arxiv.org/abs/10.3204/DESY-PROC-2009-03/Krop).
- [73] P. Mastrandrea (CDF, D0 Collaboration), Multi-boson production, in *29th International Conference on Physics in Collision* (2010), [arXiv:1009.1829](https://arxiv.org/abs/1009.1829).
- [74] V.M. Abazov *et al.* (D0 Collaboration), Limits on anomalous trilinear gauge boson couplings from WW , WZ and $W\gamma$ production in $p\bar{p}$ collisions at $\sqrt{s} = 1.96$ TeV, *Phys. Lett. B* **718**, 451 (2012).
- [75] V.M. Abazov *et al.* (D0 Collaboration), Measurement of spin correlation between top and antitop quarks produced in $p\bar{p}$ collisions at $\sqrt{s} = 1.96$ TeV, *Phys. Lett. B* **757**, 199 (2016).
- [76] C. Degrande, C. Duhr, B. Fuks, D. Grellscheid, O. Mattelaer, and T. Reiter, UFO—The universal FeynRules output, *Comput. Phys. Commun.* **183**, 1201 (2012).
- [77] A. Alloul, N. D. Christensen, C. Degrande, C. Duhr, and B. Fuks, FeynRules 2.0—A complete toolbox for tree-level phenomenology, *Comput. Phys. Commun.* **185**, 2250 (2014).
- [78] E. Leader, *Spin in Particle Physics*, Cambridge Monographs on Particle Physics, Nuclear Physics and Cosmology (Cambridge University Press, Cambridge, England, 2001).
- [79] F. Boudjema and R. K. Singh, A model independent spin analysis of fundamental particles using azimuthal asymmetries, *J. High Energy Phys.* **07** (2009) 028.
- [80] R. Rahaman and R. K. Singh, On the choice of beam polarization in $e^+e^- \rightarrow ZZ/Z\gamma$ and anomalous triple gauge-boson couplings, *Eur. Phys. J. C* **77**, 521 (2017).
- [81] R. Rahaman and R. K. Singh, Breaking down the entire spectrum of spin correlations of a pair of particles involving fermions and gauge bosons, *Nucl. Phys.* **B984**, 115984 (2022).
- [82] G. Aad *et al.* (ATLAS Collaboration), Measurement of Spin Correlation in Top-Antitop Quark Events and Search for Top Squark Pair Production in pp Collisions at $\sqrt{s} = 8$ TeV Using the ATLAS Detector, *Phys. Rev. Lett.* **114**, 142001 (2015).
- [83] G. Aad *et al.* (ATLAS Collaboration), Observation of Spin Correlation in $t\bar{t}$ Events from pp Collisions at $\sqrt{s} = 7$ TeV using the ATLAS Detector, *Phys. Rev. Lett.* **108**, 212001 (2012).
- [84] S. Neuhaus, S. Skambraks, and C. Kiesling, Track vertex reconstruction with neural networks at the first level trigger of Belle II, *EPJ Web Conf.* **150**, 00009 (2017).
- [85] B. H. Denby, Neural networks and cellular automata in experimental high-energy physics, *Comput. Phys. Commun.* **49**, 429 (1988).
- [86] L. Lonnblad, C. Peterson, and T. Rognvaldsson, Finding Gluon Jets with a Neural Trigger, *Phys. Rev. Lett.* **65**, 1321 (1990).
- [87] J. Pumplin, How to tell quark jets from gluon jets, *Phys. Rev. D* **44**, 2025 (1991).
- [88] M. Andrews, J. Alison, S. An, P. Bryant, B. Burkle, S. Gleyzer, M. Narain, M. Paulini, B. Poczos, and E. Usai, End-to-end jet classification of quarks and gluons with the CMS open data, *Nucl. Instrum. Methods Phys. Res., Sect. A* **977**, 164304 (2020).
- [89] P. T. Komiske, E. M. Metodiev, and M. D. Schwartz, Deep learning in color: Towards automated quark/gluon jet discrimination, *J. High Energy Phys.* **01** (2017) 110.
- [90] T. Cheng, Recursive neural networks in quark/gluon tagging, *Comput. Software Big Sci.* **2**, 3 (2018).
- [91] Y.-T. Chien and R. Kunnawalkam Elayavalli, Probing heavy ion collisions using quark and gluon jet substructure, [arXiv:1803.03589](https://arxiv.org/abs/1803.03589).
- [92] G. Kasieczka, N. Kiefer, T. Plehn, and J. M. Thompson, Quark-gluon tagging: Machine learning vs detector, *SciPost Phys.* **6**, 069 (2019).
- [93] J. Cogan, M. Kagan, E. Strauss, and A. Schwartzman, Jet-images: Computer vision inspired techniques for jet tagging, *J. High Energy Phys.* **02** (2015) 118.
- [94] J. S. H. Lee, I. Park, I. J. Watson, and S. Yang, Quark-gluon jet discrimination using convolutional neural networks, *J. Korean Phys. Soc.* **74**, 219 (2019).
- [95] L. G. Almeida, M. Backović, M. Cliche, S. J. Lee, and M. Perelstein, Playing tag with ANN: Boosted top identification with pattern recognition, *J. High Energy Phys.* **07** (2015) 086.
- [96] D. Guest, J. Collado, P. Baldi, S.-C. Hsu, G. Urban, and D. Whiteson, Jet flavor classification in high-energy physics with deep neural networks, *Phys. Rev. D* **94**, 112002 (2016).
- [97] E. Bols, J. Kieseler, M. Verzetti, M. Stoye, and A. Stakia, Jet flavour classification using DeepJet, *J. Instrum.* **15**, P12012 (2020).
- [98] K. Goto, T. Suehara, T. Yoshioka, M. Kurata, H. Nagahara, Y. Nakashima, N. Takemura, and M. Iwasaki, Development of a vertex finding algorithm using recurrent neural network, *Nucl. Instrum. Methods Phys. Res., Sect. A* **1047**, 167836 (2023).
- [99] J. Bielčíková, R. Kunnawalkam Elayavalli, G. Ponimatkin, J. H. Putschke, and J. Sivic, Identifying heavy-flavor jets

- using vectors of locally aggregated descriptors, *J. Instrum.* **16**, P03017 (2021).
- [100] L. de Oliveira, M. Kagan, L. Mackey, B. Nachman, and A. Schwartzman, Jet-images—deep learning edition, *J. High Energy Phys.* **07** (2016) 069.
- [101] J. Barnard, E. N. Dawe, M. J. Dolan, and N. Rajcic, Parton shower uncertainties in jet substructure analyses with deep neural networks, *Phys. Rev. D* **95**, 014018 (2017).
- [102] Y.-C. J. Chen, C.-W. Chiang, G. Cottin, and D. Shih, Boosted W and Z tagging with jet charge and deep learning, *Phys. Rev. D* **101**, 053001 (2020).
- [103] P. Baldi, P. Sadowski, and D. Whiteson, Searching for exotic particles in high-energy physics with deep learning, *Nat. Commun.* **5**, 4308 (2014).
- [104] A. Chakraborty, S. H. Lim, and M. M. Nojiri, Interpretable deep learning for two-prong jet classification with jet spectra, *J. High Energy Phys.* **07** (2019) 135.
- [105] K. Datta, A. Larkoski, and B. Nachman, Automating the construction of jet observables with machine learning, *Phys. Rev. D* **100**, 095016 (2019).
- [106] A. M. Sirunyan *et al.* (CMS Collaboration), A deep neural network to search for new long-lived particles decaying to jets, *Mach. Learn. Sci. Tech.* **1**, 035012 (2020).
- [107] J. Alimena, Y. Iiyama, and J. Kieseler, Fast convolutional neural networks for identifying long-lived particles in a high-granularity calorimeter, *J. Instrum.* **15**, P12006 (2020).
- [108] E. Bernreuther, T. Finke, F. Kahlhoefer, M. Krämer, and A. Mück, Casting a graph net to catch dark showers, *SciPost Phys.* **10**, 046 (2021).
- [109] D. Cogollo, F. F. Freitas, C. A. de S. Pires, Y. M. Oviedo-Torres, and P. Vasconcelos, Deep learning analysis of the inverse seesaw in a 3-3-1 model at the LHC, *Phys. Lett. B* **811**, 135931 (2020).
- [110] M. Grossi, J. Novak, B. Kersevan, and D. Rebuffi, Comparing traditional and deep-learning techniques of kinematic reconstruction for polarization discrimination in vector boson scattering, *Eur. Phys. J. C* **80**, 1144 (2020).
- [111] V. S. Ngairangbam, A. Bhardwaj, P. Konar, and A. K. Nayak, Invisible Higgs search through vector boson fusion: A deep learning approach, *Eur. Phys. J. C* **80**, 1055 (2020).
- [112] C. Englert, M. Fairbairn, M. Spannowsky, P. Stylianou, and S. Varma, Sensing Higgs boson cascade decays through memory, *Phys. Rev. D* **102**, 095027 (2020).
- [113] F. F. Freitas, J. Gonçalves, A. P. Morais, and R. Pasechnik, Phenomenology of vector-like leptons with deep learning at the large hadron collider, *J. High Energy Phys.* **01** (2021) 076.
- [114] F. F. Freitas, C. K. Khosa, and V. Sanz, Exploring the Standard Model EFT in VH production with machine learning, *Phys. Rev. D* **100**, 035040 (2019).
- [115] L. de Oliveira, B. Nachman, and M. Paganini, Electromagnetic showers beyond shower shapes, *Nucl. Instrum. Methods Phys. Res., Sect. A* **951**, 162879 (2020).
- [116] D. Belayneh *et al.*, Calorimetry with deep learning: Particle simulation and reconstruction for collider physics, *Eur. Phys. J. C* **80**, 688 (2020).
- [117] S. R. Qasim, J. Kieseler, Y. Iiyama, and M. Pierini, Learning representations of irregular particle-detector geometry with distance-weighted graph networks, *Eur. Phys. J. C* **79**, 608 (2019).
- [118] J. Alwall, M. Herquet, F. Maltoni, O. Mattelaer, and T. Stelzer, MadGraph 5: Going beyond, *J. High Energy Phys.* **06** (2011) 128.
- [119] T. Sjöstrand, S. Ask, J. R. Christiansen, R. Corke, N. Desai, P. Ilten, S. Mrenna, S. Prestel, C. O. Rasmussen, and P. Z. Skands, An introduction to PYTHIA 8.2, *Comput. Phys. Commun.* **191**, 159 (2015).
- [120] M. Cacciari, G. P. Salam, and G. Soyez, FastJet user manual, *Eur. Phys. J. C* **72**, 1896 (2012).
- [121] M. Cacciari and G. P. Salam, Dispelling the N^3 myth for the k_t jet-finder, *Phys. Lett. B* **641**, 57 (2006).
- [122] M. Cacciari, G. P. Salam, and G. Soyez, The anti- k_t jet clustering algorithm, *J. High Energy Phys.* **04** (2008) 063.
- [123] S. Catani, Y. L. Dokshitzer, M. H. Seymour, and B. R. Webber, Longitudinally invariant K_t clustering algorithms for hadron hadron collisions, *Nucl. Phys.* **B406**, 187 (1993).
- [124] R. L. Workman *et al.* (Particle Data Group), Review of particle physics, *Prog. Theor. Exp. Phys.* **2022**, 083C01 (2022).
- [125] T. Chen and C. Guestrin, XGBoost: A scalable tree boosting system, in *Proceedings of the 22nd ACM SIGKDD International Conference on Knowledge Discovery and Data Mining*, KDD '16 (ACM, New York, NY, USA, 2016), pp. 785–794.
- [126] Y. Nakai, D. Shih, and S. Thomas, Strange jet tagging, [arXiv:2003.09517](https://arxiv.org/abs/2003.09517).
- [127] J. Erdmann, A tagger for strange jets based on tracking information using long short-term memory, *J. Instrum.* **15**, P01021 (2020).
- [128] P. Skands, S. Carrazza, and J. Rojo, Tuning PYTHIA 8.1: The Monash 2013 Tune, *Eur. Phys. J. C* **74**, 3024 (2014).
- [129] R. Corke and T. Sjostrand, Interleaved parton showers and tuning prospects, *J. High Energy Phys.* **03** (2011) 032.
- [130] CERN, ATLAS PYTHIA 8 tunes to 7 TeV data, ATL-PHYS-PUB-2014-021, 2014.
- [131] A. Abada *et al.* (FCC Collaboration), FCC physics opportunities: Future circular collider conceptual design report volume 1, *Eur. Phys. J. C* **79**, 474 (2019).
- [132] N. Metropolis and S. Ulam, The Monte Carlo method, *J. Am. Stat. Assoc.* **44**, 335 (1949).
- [133] W. K. Hastings, Monte Carlo sampling methods using Markov chains and their applications, *Biometrika* **57**, 97 (1970).
- [134] A. Lewis, getdist: A Python package for analysing Monte Carlo samples, [arXiv:1910.13970](https://arxiv.org/abs/1910.13970).